Neurobiology of Disease

ZCCHC17 Modulates Neuronal RNA Splicing and Supports Cognitive Resilience in Alzheimer's Disease

Anne Marie W. Bartosch,[1,2] Elliot H. H. Youth,[1,2] Shania Hansen,[3,4] Yiyang Wu,[3,4] Heather M. Buchanan,[1,2] Maria E. Kaufman,[2] Harrison Xiao,[1,2] So Yeon Koo,[2] Archana Ashok,[2] Sharanya Sivakumar,[1,2] Rajesh K. Soni,[5] Logan C. Dumitrescu,[3,4] Tiffany G. Lam,[1,2] Ali S. Ropri,[1,2] Annie J. Lee,[2,6] Hans-Ulrich Klein,[2,6] Badri N. Vardarajan,[2,7] David A. Bennett,[8] Tracy L. Young-Pearse,[9,10] Philip L. De Jager,[2,6] Timothy J. Hohman,[3,4] Andrew A. Sproul,[1,2] and Andrew F. Teich[1,2,7]

[1]Department of Pathology and Cell Biology, Columbia University Irving Medical Center, New York, New York 10032, [2]Taub Institute for Research on Alzheimer's Disease and the Aging Brain, Columbia University Irving Medical Center, New York, New York 10032, [3]Department of Neurology, Vanderbilt Memory & Alzheimer's Center, Vanderbilt University Medical Center, Nashville, Tennessee 37232, [4]Vanderbilt Genetics Institute, Vanderbilt University Medical Center, Nashville, Tennessee 37232, [5]Proteomics and Macromolecular Crystallography Shared Resource, Herbert Irving Comprehensive Cancer Center, New York, New York 10032, [6]Department of Neurology, Center for Translational & Computational Neuroimmunology, Columbia University Irving Medical Center, New York Presbyterian Hospital, New York, New York 10032, [7]Department of Neurology, Columbia University Irving Medical Center, New York Presbyterian Hospital, New York, New York 10032, [8]Rush Alzheimer's Disease Center, Rush University Medical Center, Chicago, Illinois 60612, [9]Department of Neurology, Ann Romney Center for Neurologic Diseases, Brigham and Women's Hospital and Harvard Medical School, Boston, Massachusetts 02115, and [10]Harvard Stem Cell Institute, Harvard University, Cambridge, Massachusetts 02138

ZCCHC17 is a putative master regulator of synaptic gene dysfunction in Alzheimer's disease (AD), and ZCCHC17 protein declines early in AD brain tissue, before significant gliosis or neuronal loss. Here, we investigate the function of ZCCHC17 and its role in AD pathogenesis using data from human autopsy tissue (consisting of males and females) and female human cell lines. Co-immunoprecipitation (co-IP) of ZCCHC17 followed by mass spectrometry analysis in human iPSC-derived neurons reveals that ZCCHC17's binding partners are enriched for RNA-splicing proteins. ZCCHC17 knockdown results in widespread RNA-splicing changes that significantly overlap with splicing changes found in AD brain tissue, with synaptic genes commonly affected. ZCCHC17 expression correlates with cognitive resilience in AD patients, and we uncover an APOE4-dependent negative correlation of ZCCHC17 expression with tangle burden. Furthermore, a majority of ZCCHC17 interactors also co-IP with known tau interactors, and we find a significant overlap between alternatively spliced genes in ZCCHC17 knockdown and tau overexpression neurons. These results demonstrate ZCCHC17's role in neuronal RNA processing and its interaction with pathology and cognitive resilience in AD, and suggest that the maintenance of ZCCHC17 function may be a therapeutic strategy for preserving cognitive function in the setting of AD pathology.

Key words: **Alzheimer's; iPSC; neurons; synaptic; ZCCHC17**

Significance Statement

Abnormal RNA processing is an important component of AD pathophysiology. We show here that ZCCHC17, a previously identified putative master regulator of synaptic dysfunction in AD, plays a role in neuronal RNA processing, and illustrate that ZCCHC17 dysfunction is sufficient to explain some of the splicing abnormalities seen in AD brain tissue, including synaptic gene splicing abnormalities. Using data from human patients, we demonstrate that ZCCHC17 mRNA levels correlate with cognitive resilience in the setting of AD pathology. These results suggest that maintenance of ZCCHC17 function may be a therapeutic strategy for supporting cognitive function in AD patients, and motivate future work examining a possible role of abnormal RNA processing in AD-related cognitive decline.

Received Dec. 20, 2022; revised Sept. 22, 2023; accepted Nov. 7, 2023.

Author contributions: A.B., E.Y., A.S., and A.T. designed research; A.B., E.Y., H.B., M.K., H.X., S.K., A.A., S.S., and R.S. performed research; A.B., E.Y., S.H., Y.W., H.B., R.S., L.D., T.L., A.R., A.L., H.K., B.V., T.H., A.S., and A.T. analyzed data; A.B., E.Y., and A.T. wrote the paper.

This work is supported by the National Institutes of Health–National Institute on Aging Grants R03AG048077 and R01AG059854 and the Alzheimer's Association Grant NIRG-13-283742 for A.T. A.S. is supported by Co-Investigator (R01AG059854), the Thompson Family Foundation (TAME-AD), and The Henry and Marilyn Taub Foundation. The Religious Orders Study and Rush Memory and Aging Project is supported by the National Institutes of Health–National Institute on Aging Grants P30AG10161, P30AG72975, R01AG15819, R01AG17917, U01AG46152, and U01AG61356. We thank the Electrophysiology Core Facility, Center for Translational Research in Neurodevelopmental Disease, Columbia University Irvine Medical Center for their help in conducting electrophysiological experiments to assess the functional activity of our NPC-derived neurons.

The authors declare no competing financial interests.

Correspondence should be addressed to Andrew F. Teich at aft25@cumc.columbia.edu.

https://doi.org/10.1523/JNEUROSCI.2324-22.2023

Introduction

Synaptic dysfunction linked to cognitive performance is an early occurrence in AD animal models (Trinchese et al., 2004; Smith et al., 2009; Siskova et al., 2014), and dysregulation of synaptic gene expression has consistently been shown in AD autopsy tissue (Loring et al., 2001; Colangelo et al., 2002; Liang et al., 2008). Understanding the molecular basis of synaptic dysfunction is therefore of high importance in the AD field (Teich et al., 2015). We previously used mutual information relationships between RNA expression profiles of autopsy brain tissue to identify transcriptional regulators that may be driving dysregulated synaptic gene transcription in AD, and reported ZCCHC17 as a candidate regulator that is predicted to have reduced activity in AD, leading to dysregulation of gene expression across a broad range of categories (including synaptic) (Tomljanovic et al., 2018). ZCCHC17 was discovered in 2002 while screening a cDNA library for RNA-binding proteins (Gueydan et al., 2002) and was also independently found in 2003 using a yeast two-hybrid screen that searched for pinin-interacting proteins (Chang et al., 2003). Additionally, ZCCHC17 interacts with SRrp37, which regulates splicing of pre-mRNA (Ouyang, 2009), and has recently been shown to interact with the splicing factors SRSF1 and SRSF2 (Lin et al., 2017). ZCCHC17 contains an S1 RNA-binding domain, zinc-finger (CCHC) domain, and two nuclear localization signals, and Northern blot analysis has shown that its transcripts are found throughout the body, with the strongest expression in the normal brain, heart, skeletal muscle, and thymus (Chang et al., 2003). Although the exact function of ZCCHC17 is unknown, recent evidence showing that it is involved in mRNA (Lin et al., 2017) and rRNA (Lin et al., 2019) processing have led some to suggest that it may help coordinate a wide range of homeostatic functions in the cell (Lin et al., 2017). Our prior work demonstrated that ZCCHC17 protein is expressed in neurons and declines early in AD brain tissue before significant gliosis or neuronal loss, while knockdown of ZCCHC17 in rat neuronal cultures leads to dysregulation of a wide range of genes, including synaptic genes (Tomljanovic et al., 2018). ZCCHC17 has been bioinformatically linked to AD more generally by others as well (Li et al., 2015). However, the activity of ZCCHC17 in human neurons has not yet been explored, and its clinical relevance in AD patients has not been examined.

Here, we investigate the functional role of ZCCHC17 in a human iPSC (hiPSC)-derived neuronal model, and explore how this role may contribute to a clinical decline in AD patients. By performing co-immunoprecipitation (co-IP) of ZCCHC17 in human neurons followed by mass spectrometry analysis, we show that ZCCHC17 interacts with a network of splicing proteins. Furthermore, ZCCHC17 knockdown leads to dysregulation of mRNA splicing across a broad range of gene categories (including synaptic), and these differentially spliced genes (DSGs) overlap significantly with those seen in AD brain tissue. ZCCHC17 expression correlates with cognitive resilience in AD patients through two different approaches [using Religious Orders Study and Rush Memory and Aging Project (ROSMAP) data and PrediXcan analysis], and we uncover an APOE4-dependent correlation of ZCCHC17 expression with neurofibrillary tangle burden. Finally, we show that a majority of ZCCHC17 interactors identified by co-IP also co-IP with known tau interactors, and we find significant overlap between alternatively spliced genes in ZCCHC17 knockdown and tau overexpression neurons. Taken together, the above results support a role for ZCCHC17 in neuronal RNA-splicing and cognitive resilience in AD and point to tau as a possible mediator of ZCCHC17 dysfunction.

Materials and Methods

hiPSC and neuronal cell culture and quality control. All human cell line work was performed on de-identified cell lines and approved by the Columbia University Institutional Review Board (IRB). IMR90 cl.4 hiPSCs (WiCell; sex genotype XX) (Yu et al., 2007, 2009; Chen et al., 2011; Hu et al., 2011) were grown in StemFlex media (Thermo Scientific) on Cultrex (Bio-Techne) and passaged with ReLeSR as described previously (Song et al., 2021). Human neural progenitor cells (NPCs) were generated using dual SMAD inhibition as nonadherent embryoid bodies, followed by plating on polyornithine (10 µg/ml, Sigma P4957)/laminin (10 µg/ml, R&D Systems 3400-010-02) and subsequent manual rosette selection and expansion, as described previously (Topol et al., 2015; Sun et al., 2019). NPCs were maintained on Matrigel (Corning 354230) and split 1:2 to 1:3 every 5–7 days. Neuronal differentiations were carried out by plating 200,000 cells/12 well-well or 500,000 cells/6 well-well in DMEM/F12 base media (Gibco 11320-033) supplemented with B27 (Gibco 17504-044), N2 (Gibco 17502-048), penicillin/streptomycin (Gibco 15140-122), BDNF (20 ng/ml, R&D Systems 248-BDB), and laminin (1 µg/ml). After 1 week of differentiation, AraC (Tocris 4520) was added at 100 nM to reduce the remaining NPC proliferation. Neurons were differentiated for 6–11 weeks post-NPC stage.

Our previously published work using a related differentiation protocol indicated that neurons should have sufficient electrophysiological maturity at these time points (Pre et al., 2014). To quality control neuronal differentiations using this cell line and differentiation protocol, we performed immunofluorescence which showed expression of synaptophysin and MAP2, and demonstrated the capacity for action potentials via patch electrophysiology (Extended Data Fig. 1-1). Immunofluorescence methods are described below. Electrophysiologic recordings were carried out using conventional whole-cell current clamp using a Multiclamp 700B amplifier and a Digidata 1550 digital-to-analog converter. Signals were recorded at a 10 kHz sample rate and filtered at 3 kHz with low-pass Bessel filter using pClamp 10 software (all equipment from Molecular Devices). The external recording solution contained 145 mM NaCl, 5 mM KCl, 10 mM HEPES, 10 mM glucose, 2 mM $CaCl_2$ and 2 mM $MgCl_2$. The pH was adjusted to 7.3 using NaOH, and the osmolality adjusted to 325 mOsm with sucrose. The pipette solution contained 130 mM CH_3KO_3S, 10 mM CH_3NaO_3S, 1 mM $CaCl_2$, 10 mM EGTA, 10 mM HEPES, 5 mM MgATP, and 0.5 mM Na_2GTP (pH 7.3, 305 mOsm). Experiments were performed at room temperature (21–23° C). A −14 mV liquid junction potential between the pipette and external solutions was calculated empirically, and the correction were applied before the experiment. Only the cells with a stable series resistance of <15 MΩ were used for analysis. During recordings, current (<100 pA) was manually injected to hold the cells at approximately −70 mV. Action potentials were evoked using 1 s duration depolarizing current steps that increased incrementally by 5 pA. An action potential was defined as a transient depolarization of the membrane which had a minimum rise rate of >10 mV/ms and reached a peak amplitude of >0 mV. Quantification was carried out using custom written scripts for Igor Pro v. 6 (WaveMetrics) and R v. 3 (www.R-project.org).

Lentiviral construct and lentiviral particle formation. cDNA corresponding to human ZCCHC17 transcript variant 3 was ordered from the MGC Collection from Dharmacon (Horizon Discovery Biosciences MHS6278-202760302). This was used as a template for PCR using Amplitaq Gold (Life Technologies, as per user instructions), utilizing the following primers that introduced a Kozak sequence and an N-terminal FLAG sequence after the translational start site: ZCC_NFLAG_TOPO_F:CACCATGGACTACAAAGACGATGACGACAAGAATTCAGGAAGGCCTGAGACC, ZCC_NFLAG_TOPO_R:TCACTCCTTGTGCTTCTTCTTGTGC.

Purified PCR products were then TOPO-cloned into pENTRE/D-TOPO (Life Technologies). Transformed bacterial colonies (Stb3, Life Technologies) were miniprepped (Qiagen) and confirmed to be correct by Sanger sequence (Genewiz/Azenta). One correct clone was subsequently Gateway-cloned (Life Technologies, as per user instructions) into pLEX-305, which was a gift from David Root (Addgene plasmid 41390; http://n2t.net/addgene:41390; RRID:Addgene_41390). Transformed bacterial colonies were miniprepped and confirmed to be correct by Sanger sequence, and then midiprepped (Machery-Nagel) for use in lentiviral particle generation. A similar strategy was later used for C-terminal tagged ZCCHC17, using the following primers: ZCC_CFLAG_TOPO_F:CACCATGAATTCAGGAAGGCCTGAGACC, ZCC_CFLAG_TOPO_R:TCACTTGTCGTCATCGTCTTTGTAGTCCT CCTTGTGCTTCTTCTTGTGC.

"True empty" pLEX-305 was generated by excision of the ccdB8 selection cassette using Age1 and Xho1 restriction digest, blunting via Large Klenow Fragment, and gel purification of the digested plasmid (2,243 bp excised), followed by blunt ligation and bacterial transformation. After the bacterial colonies were miniprepped and confirmed to be correct by Sanger sequence, a correct clone was midiprepped for lentiviral particle production.

Lentiviral particles from N- and C-terminal FLAG-tagged ZCCHC17 as well as empty pLEX_305 vector were generated as described previously (Song et al., 2021). Briefly, HEK 293T cells were plated at 180,000 cells/cm^2 on gelatin-coated 15 cm plates and fed with 20 ml FM10 media. Cells were confirmed to be 80–90% confluent preceding transfection the following day. An 80 µl of Lipofectamine 3000 (Invitrogen L3000-015) was mixed with 2 ml Opti-MEM (Gibco 31985-070) in a 15 ml conical tube and vortexed for 3 s. A plasmid DNA master mix was prepared in a separate 15 ml conical tube, comprising 20 µg of FLAG-ZCCHC17, ZCCHC17-FLAG, or control pLEX_305 empty vector, 15 µg of psPAX2 (Addgene #12260), and 10 µg of VSV-G (Addgene 14888) in 2 ml of Opti-MEM, supplemented with 80 µl of P3000 reagent (Invitrogen L3000-015). The two mixes were combined and incubated at room temperature for 10 min, and the transfection mixture was subsequently pipetted onto cells in a dropwise manner. Cells were then incubated for 5–6 h at 37°C, after which the transfection media was replaced with 18.5 ml of fresh FM10. The viral supernatants were collected 48 and 72 h post-transfection and centrifuged for 3 min at 300 × *g*. The supernatants were then combined, vacuum-filtered, transferred to new tubes, supplemented with 1/3 volume Lenti-X Concentrator (Takara 631232), mixed by gentle inversion, and incubated overnight at 4°C. The following day, the samples were centrifuged for 45 min at 4°C at 1,500 × *g*. The supernatants were removed, and the lentiviral pellets were resuspended in DPBS (Gibco 14190-044) and stored at −80°C.

Immunofluorescence. The hiPSC-derived neurons on glass coverslips in 12-well plates were infected with FLAG-tagged ZCCHC17 and control lentivirus 1 week prior to fixation and immunostained to assess the expression of constructs via immunofluorescence. Cells were fixed in 4% paraformaldehyde for 20 min, incubated with 0.2% Triton X-100 (Thermo 85111) in PBS for 5 min, and washed three times with PBS. Coverslips were incubated for 1 h at room temperature in blocking solution, consisting of 5% goat serum in PBS, and then overnight at 4°C in primary antibody solution, consisting of anti-ZCCHC17 (1:1,000, Abcam ab80454) and anti-FLAG (1:1,000, Sigma F3165) in blocking solution. Uninfected neurons were also stained in order to assess functional maturity with anti-synaptophysin (1:500, Abcam AB32127) or anti-MAP2 (1:500, Aves MAP-0020). Coverslips were rinsed three times with PBS, incubated with 1:1,000 secondary antibody in blocking solution for 1 h at room temperature, and washed three times with PBS. Coverslips were incubated for 5 min with DAPI in PBS, washed once with PBS, mounted with Vectashield (Vector H-1000), and stored at 4°C. Imaging was carried out using an LSM 800 confocal microscope (Zeiss) or Revolve microscope (Echo).

Immunoprecipitation. The hiPSC-derived neurons were differentiated in 6-well plates and infected with FLAG-tagged ZCCHC17 and control lentivirus 1 week prior to immunoprecipitation. Cells were rinsed two times with cold PBS, incubated on ice for 15 min with cold IP lysis buffer (Thermo 87787) supplemented with protease and phosphatase inhibitors (Thermo 1861280), collected into tubes by scraping, and centrifuged at 12,000 × *g* for 10 min. A 40 µl/sample of anti-FLAG conjugated magnetic bead slurry (Sigma M8823) was prepared by washing six times with PBS to remove glycerol from beads. Lysates were diluted to 1 ml total volume with additional IP lysis buffer with inhibitors. Anti-FLAG beads were added to the samples, gently mixed, and incubated at room temperature on a rotator for 2 h. Anti-FLAG beads with bound sample were magnetically separated from the remaining unbound sample and rinsed two times with 1 ml PBS. The immunoprecipitated samples were further processed by *in-gel* digestion for mass spectrometry or prepared for Western blotting as detailed below.

Western blotting. Tris-glycine SDS sample buffer (Thermo LC2676) was added to beads with bound sample and boiled for 3 min. Bound sample in sample buffer was magnetically separated from beads and stored at −80°C. Thawed samples were supplemented with sample reducing agent (Thermo NP0009), and boiled for 5 min prior to loading to 4–20% gradient gels (Thermo XP04200BO). The samples were separated by SDS-PAGE and transferred to nitrocellulose membrane at 30 V overnight at 4°C. The membranes were incubated for 1 h in 100% sea block blocking buffer (Thermo 37527) on a rocker at room temperature. Anti-FLAG (1:1,000, Sigma F3165), anti-ZCCHC17 (1:1,000, Abcam ab80454), anti-AP2A1 (1:1,000, Proteintech 11401-1-AP), anti-hnRNPU (1:1,000, ABclonal A3917), anti-VMP1 (1:1,000, CST 12929S), anti-p62 (1:1,000, BioLegend 814802), or anti-GAPDH (1:1,000, Abcam ab9485) were added to 50% sea block in TBS-Tween (TBST) buffer solution and incubated at 4°C overnight with rocking. After washing with TBST, secondary antibodies (LI-COR or Thermo A16096) were added at 1:10,000 to 50% sea block in TBST and incubated for 1 h at room temperature with rocking. The membranes were washed and imaged using the LI-COR Odyssey imaging system for fluorescence or the Bio-Rad ChemiDoc imaging system for enhanced chemiluminescence.

In-gel digestion for mass spectrometry. The immunoprecipitated samples ($n = 3$ per group, including FLAG-ZCCHC17, ZCCHC17-FLAG, and negative control samples) were separated on 4–12% gradient SDS-PAGE and stained with SimplyBlue. Protein gel slices were excised and *in-gel* digestion was performed as previously described (Shevchenko et al., 2006), with minor modifications. Each gel slice was washed with 1:1 acetonitrile and 100 mM ammonium bicarbonate for 30 min, and then dehydrated with 100% acetonitrile for 10 min until shrunk. The excess acetonitrile was then removed, and the slice was dried in a speed-vacuum at room temperature for 10 min. The gel slice was reduced with 5 mM DTT for 30 min at 56°C in an air thermostat, cooled down to room temperature, and alkylated with 11 mM IAA for 30 min with no light. The gel slice was then washed with 100 mM ammonium bicarbonate and 100% acetonitrile for 10 min each. Excess acetonitrile was removed and dried in a speed-vacuum for 10 min at room temperature, after which the gel slice was re-hydrated in a solution of 25 ng/µl trypsin in 50 mM ammonium bicarbonate for 30 min on ice and digested overnight at 37°C in an air thermostat. Digested peptides were collected and further extracted from the gel slice in extraction buffer (1:2 ratio by volume of 5% formic acid:acetonitrile) by shaking at high speed in an air thermostat. The supernatants from both extractions were then combined and dried in a speed-vacuum. Peptides were dissolved in 3% acetonitrile/0.1% formic acid.

Liquid chromatography with tandem mass spectrometry. Desalted peptides were injected in an EASY-Spray PepMap RSLC C18 50 cm × 75 cm ID column (Thermo Scientific) connected to an Orbitrap Fusion Tribrid (Thermo Scientific). Peptide elution and separation was achieved at a nonlinear flow rate of 250 nl/min using a gradient of 5–30% of buffer B [0.1% (v/v) formic acid, 100% acetonitrile] for 110 min, with column temperature maintained at 50°C throughout the entire experiment. The Thermo Scientific Orbitrap Fusion Tribrid

mass spectrometer was used for peptide tandem mass spectroscopy (MS/MS). Survey scans of peptide precursors were performed from 400 to 1,500 m/z at 120 K full width at half maximum (FWHM) resolution (at 200 m/z) with a 2×10^5 ion count target and a maximum injection time of 50 ms. The instrument was set to run in top speed mode with 3 s cycles for the survey and the MS/MS scans. After a survey scan, MS/MS was performed on the most abundant precursors, that is, those exhibiting a charge state from 2 to 6 of greater than 5×10^3 intensity, by isolating them in the quadrupole at 1.6 Th. We used collision-induced dissociation (CID) with 35% collision energy and detected the resulting fragments with the rapid scan rate in the ion trap. The automatic gain control (AGC) target for MS/MS was set to 1×10^4, and the maximum injection time was limited to 35 ms. The dynamic exclusion was set to 45 s with a 10 ppm mass tolerance around the precursor and its isotopes. Monoisotopic precursor selection was enabled.

Liquid chromatography with tandem mass spectrometry analysis. Raw mass spectrometric data were analyzed using the MaxQuant environment (v1.6.1.0) and Andromeda for database searches (Cox et al., 2011) at default settings with a few modifications. The default was used for the first search tolerance and main search tolerance (20 ppm and 6 ppm, respectively). MaxQuant was set up to search with the reference human proteome database downloaded from Uniprot (https://www.uniprot.org/proteomes/UP000005640). MaxQuant performed the search for trypsin digestion with up to two missed cleavages. Peptide, site, and protein false discovery rates (FDR) were all set to 1% with a minimum of one peptide needed for identification; label-free quantitation (LFQ) was performed with a minimum ratio count of 1. The following modifications were used for protein quantification: oxidation of methionine (M), acetylation of the protein N-terminus, and deamination for asparagine or glutamine (NQ). The results obtained from MaxQuant were further analyzed using R. Protein identifications were filtered for common contaminants. Proteins were considered for quantification only if they were found in at least two replicate samples from a test group. Significant enrichment in protein abundance was determined by *t* test with a significance threshold of adjusted *p*-value of <0.1 (permutation-based FDR correction) and $\log_2$(FoldChange) >0.3.

ZCCHC17 siRNA delivery. The hiPSC-derived neurons were fed and treated with 1 μM Accell self-delivering siRNA, consisting of a pool of four unique ZCCHC17 sequences (Horizon Discovery Biosciences E-105851-00) or four nontargeting control sequences (Horizon Discovery Biosciences D-001910-10). Cells were harvested 7 d after siRNA treatment for corresponding experiments.

RNA extraction. The hiPSC-derived neurons were lysed in Qiazol lysis reagent (Qiagen 79306) on ice and frozen at −80°C. A total of 12 samples were collected for RNA sequencing ($n = 6$ ZCCHC17 knockdown biological replicates and $n = 6$ negative control biological replicates). RNA was extracted using the miRNeasy Mini kit (Qiagen 217004). RNA library preparation and sequencing were conducted at GENEWIZ, LLC (South Plainfield, NJ, USA) as described below.

Library preparation with stranded PolyA selection. Total RNA samples were quantified using a Qubit 2.0 Fluorometer (Life Technologies), and RNA integrity was checked by an Agilent TapeStation 4200 (Agilent Technologies). RNA sequencing libraries were prepared using the NEBNext Ultra II Directional RNA Library Prep Kit for Illumina, following the manufacturer's instructions (NEB). Briefly, mRNAs were first enriched with Oligo(dT) beads, and enriched mRNAs were fragmented for 15 min at 94°C. First-strand and second-strand cDNAs were subsequently synthesized. cDNA fragments were end-repaired and adenylated at their 3' ends, and universal adapters were ligated to the cDNA fragments, followed by index addition and library enrichment by limited-cycle PCR. The sequencing libraries were validated on an Agilent TapeStation (Agilent Technologies), and quantified using a Qubit 2.0 Fluorometer (Invitrogen) as well as by quantitative PCR (KAPA Biosystems).

HiSeq sequencing. The sequencing libraries were pooled and clustered on four lanes of a flowcell. After clustering, the flowcell was loaded on an Illumina HiSeq instrument (4,000 or equivalent) according to the manufacturer's instructions. The samples were sequenced using a 2 × 150 bp paired-end (PE) configuration. Image analysis and base calling was performed by the HiSeq Control Software (HCS). Raw sequence data (.bcl files) generated from Illumina HiSeq was converted into fastq files and de-multiplexed using Illumina's bcl2fastq 2.17 software. One mismatch was allowed for index sequence identification.

RNA sequencing data preprocessing. Raw RNA-seq data for ZCCHC17 knockdown neurons (IMR90 cell lines, sex genotype XX), ROSMAP bulk dorsolateral prefrontal cortex (DLPFC) tissue (433 females, 247 males) (Bennett et al., 2018; Mostafavi et al., 2018), and tau overexpression neurons (YZ1 clone of IMR-90; sex genotype XX) (Raj et al., 2018) were preprocessed as follows. The quality of all FASTQ files was assessed using FastQC (v0.11.9), and all samples for which one or both paired-end FASTQ files failed the "per base sequencing quality" metric were excluded from downstream analysis in order to ensure confidence in sequence-based inferences. Reads were aligned to the GRCh38 genome (Ensembl Release 101) using STAR (v2.7.6a) in two-pass mapping mode with standard ENCODE parameters. Gene counts were quantified from STAR-aligned BAM files using featureCounts (v2.0.1). Only samples with RIN ≥ 5 were used for downstream analysis.

RNA-splicing analysis. Differential splicing analysis was performed using LeafCutter (v0.2.9) in Python (v2.7) and R (v3.4.4) (Li et al., 2018). LeafCutter enables annotation-agnostic quantification of RNA splicing by grouping introns inferred from aligned reads into splicing clusters which enable statistical comparison of differential usage between two groups. We chose parameters that were designed to detect a wide range of splicing events, but that also required any tested splicing events to be present at a moderate baseline threshold in order to enhance reliability. In brief, splicing events were extracted from STAR-aligned BAM files using regtools (v0.5.2) with a minimum anchor length of 8 bp, minimum intron length of 20 bp, and maximum intron length of 1 Mbp. The resulting junction files were then clustered with LeafCutter, allowing introns of maximum length of 1 Mbp and requiring each intron to be supported by at least 100 reads and account for at least 5% of the reads in its splicing cluster. Differential splicing analysis was performed by LeafCutter, requiring that each intron analyzed be supported by at least 30 reads in all samples (for NPC-derived neurons and tau overexpression neurons) or in at least half of the samples in each clinical diagnosis group (for ROSMAP bulk DLPFC tissue). Differential splicing in ROSMAP was assessed between AD samples (defined as those with a clinical diagnosis of Alzheimer's dementia and no other cause of cognitive impairment) and control samples (defined as those with no cognitive impairment on clinical assessment), controlling for covariates including study (ROS or MAP), sequencing batch and depth, donor age and sex, PMI, and RIN. Downstream analysis of differential splicing results was performed in R (v4.0.2). Differentially spliced clusters were identified by FDR-corrected *p*-value of <0.05. DSGs were inferred from differentially spliced clusters which corresponded unambiguously to a single annotated gene. Individual splice junction plots were generated using LeafViz (v0.1.0). Intron usage plots were generated using ggplot2 (v3.3.2).

Gene ontology analysis. DSGs were extracted from LeafCutter analysis results as described above. Gene ontology (GO) terms spanning GO levels 2–5, and all three GO families (biological process, molecular function, and cellular component) were characterized using the "over-representation analysis" function of the ConsensusPathDB web tool. Significantly enriched GO terms were identified by FDR-corrected *p*-value of <0.05.

Nonsense-mediated decay analysis. Differential isoform analysis was performed using the IsoformSwitchAnalyzeR package (v1.10.0) in

R (v4.0.2). In brief, transcript counts were quantified from STAR-aligned BAM files using Salmon (v1.4.0), and differential isoform usage was assessed using DEXSeq. Differential isoform usage in ROSMAP samples was assessed controlling for covariates including study (ROS or MAP), sequencing batch and depth, donor age and sex, PMI, and RIN. Premature termination codons (PTCs) were defined as annotated STOP codons located at least 50 bp upstream of the final canonical exon–exon junction for a given transcript, and isoforms containing PTCs were classified as nonsense-mediated decay (NMD) sensitive. For each data set analyzed, significant changes in differential isoform fraction (dIF) were assessed using two-sided *t* tests, and associations between PTC status and dIF sign were assessed using Fisher's exact test. NMD sensitivity plots were generated using ggplot2 (v3.3.2).

Gene expression correlational analysis. ROSMAP sample metadata including APOE genotype, cognitive metrics, and midfrontal cortex AD pathology metrics were obtained from the Rush Alzheimer's Disease Center (Bennett et al., 2018; De Jager et al., 2018). All downstream analysis was performed in R (v4.0.2). After filtering out low-expression genes (defined as all those with <5 raw read counts in at least 90% of all samples), raw gene counts were normalized and variance-stabilized using DESeq2 (v1.28.1). The effects of sequencing batch and depth, donor age and sex, PMI, and RIN were subsequently regressed out using limma::removeBatchEffect (v3.44.3). Processed ZCCHC17 expression values were then Spearman-correlated to cognitive and AD pathology metrics using Hmisc::rcorr (v4.4.2). Separate analyses were run on the subset of samples with documented APOE genotypes to assess correlations for subgroups with and without the APOE4 risk factor allele. Correlational *p*-values were BH-adjusted within each analysis.

Predicted gene expression association with resilience. We leveraged data from a published genome-wide association study (GWAS) of resilience to AD neuropathology (Dumitrescu et al., 2020), defined as better-than-predicted cognitive performance given an individual's amyloid burden. PrediXcan (Gamazon et al., 2015) was used to quantify predicted levels of ZCCHC17 expression leveraging the GTEx database for model building and applied using GWAS data. Tissue-specific expression models were built leveraging elastic-net regression in the cis gene region (within 1 Mb) and selected based on fivefold cross-validation as previously described (Gamazon et al., 2015). To determine whether genetic regulation of ZCCHC17 was related to resilience, we quantified the association between predicted ZCCHC17 expression with our published Combined Resilience trait ($n = 5{,}108$) (Dumitrescu et al., 2020) covarying for age and sex. The FDR procedure was used to correct for multiple comparisons. The Generalized Berk–Jones (GBJ) test was used to summarize the association across tissues into a single test statistic. Secondary analyses were performed removing individuals with AD from the analytical model ($n = 3{,}818$). Finally, for all cross-validated ZCCHC17 models that related to resilience, we also assessed whether genetic regulation predicted observed transcript expression of ZCCHC17 in three brain regions, leveraging the genotype and RNA sequencing data from ROSMAP. All validation models were limited to non-Hispanic white participants without AD ($n = 172$) to align with the prediction models built in GTEx. For our GWAS analysis, nominally significant SNPs ($p < 1 \times 10^{-5}$) associated with AD were highlighted from summary statistics from (Jansen et al., 2019), which uses GRCh37.

snRNA-seq analysis. The analysis utilized recently published single-cell transcriptomes derived from DLPFC tissues of 424 donors (288 female, 136 male) collected at Rush Alzheimer's Disease Center (Sun et al., 2023). The processed single-cell RNA sequencing data was acquired from AD Knowledge Portal (syn2580853). Negative binomial lognormal mixed models implemented in the NEBULA (v1.2.0) R package were used to detect differential expression between clinical AD cases and cognitively normal controls. Genes with expressions in a minimum of 10% of all cells were used for the model. Cells were removed if they counted more than 20,000 or less than 200 total RNA UMIs, or had more than 5% mitochondrially mapped reads. Correction for multiple comparisons was completed using the FDR procedure (FDR < 0.05).

Results

Identification of binding partners of ZCCHC17

ZCCHC17 has been studied in non-neuronal tissues and has been shown to play a diverse range of regulatory roles in RNA processing (Lin et al., 2017, 2019). Its function has not been previously studied in human neurons, and it may exert its regulatory effect through its CCHC-type zinc-finger domain, the RNA-binding capacity of its S1 domain, or via its interactions with proteins involved in RNA processing [Fig. 1*A*; note that it may be less likely to act as a classical zinc-finger transcription factor as it only contains a single zinc-finger domain (Lambert et al., 2018)]. Since protein function is directly related to protein–protein interactions, we first performed immunoprecipitation–mass spectrometry to identify the binding partners of ZCCHC17 and elucidate its function. N- and C-terminal FLAG-tagged ZCCHC17 lentiviral constructs were expressed in human iPSC-derived neurons to enable isolation of ZCCHC17 protein and its interactors by FLAG immunoprecipitation (Extended Data Figs. 1-2, 1-3). Immunoprecipitated proteins were identified using mass spectrometry. Significant binding partners were identified by comparing proteins bound to FLAG-tagged ZCCHC17, immunoprecipitated from either FLAG-ZCCHC17- or ZCCHC17-FLAG-expressing neurons, to proteins nonspecifically bound to FLAG beads in control neurons expressing an empty vector (Fig. 1*B*,*C*). FLAG tag location (C-terminal or N-terminal) had only a marginal effect on binding partner hits; there was a significant change in the abundance of only one protein, FTL, which binds to N-terminal FLAG-tagged ZCCHC17 to a higher degree than to C-terminal FLAG-tagged ZCCHC17. This suggests that the C-terminal FLAG tag may have generated some steric hindrance which impeded FTL's ability to bind to ZCCHC17, although FTL remained a significant binding partner in both experiments when compared to control samples.

A total of 91 unique binding partners for ZCCHC17 were identified in human iPSC-derived neurons (Fig. 1*D*, Extended Data Table 1-1). Seven of these proteins have been previously identified as ZCCHC17 binding partners in non-neuronal cells, including PNN (Chang et al., 2003; Huttlin et al., 2017; Lin et al., 2017), UBTF (Lin et al., 2019), JMJD6, FTL, SRRM2, NOS1AP, and RNPS1 (Huttlin et al., 2017), suggesting conserved interactions across cell types. Several of ZCCHC17's binding partners have previously been highlighted for their importance in AD, including those involved in autophagy/lysosome function (AP2A1, AP2A2, ATP6V1A) (Raj et al., 2018; Wang et al., 2021a), stress granules (PABPC1, PABPC3) (Anderson and Kedersha, 2008), TIA-1 interactors (RPL6, RPL7, RPL7A, RPL10A, RPL13, RPS4X, AP2A1, AP2B1, ATP6V1A, PURA, SYNCRIP, PABPC1) (Vanderweyde et al., 2016), and RNA binding (ACIN1, SNRPB2) in the presence of AD pathology (Apicco et al., 2019). AP2A1 and HNRNPU were also shown by Western blot following immunoprecipitation of FLAG-tagged ZCCHC17 (Extended Data Fig. 1-4).

Enrichment analysis was performed using STRING (v11.0b), which integrates well-known classification systems including KEGG, Reactome, and Gene Ontology (Fig. 1*D*) (Szklarczyk et al., 2019). Significantly enriched GO terms included numerous RNA-processing pathways such as RNA binding, RNA splicing, and NMD (strength = 1.0, 0.8, 1.9; FDR-adjusted *p*-values for enrichment = 4.4×10^{-51}, 5.0×10^{-5}, 1.0×10^{-72}, respectively).

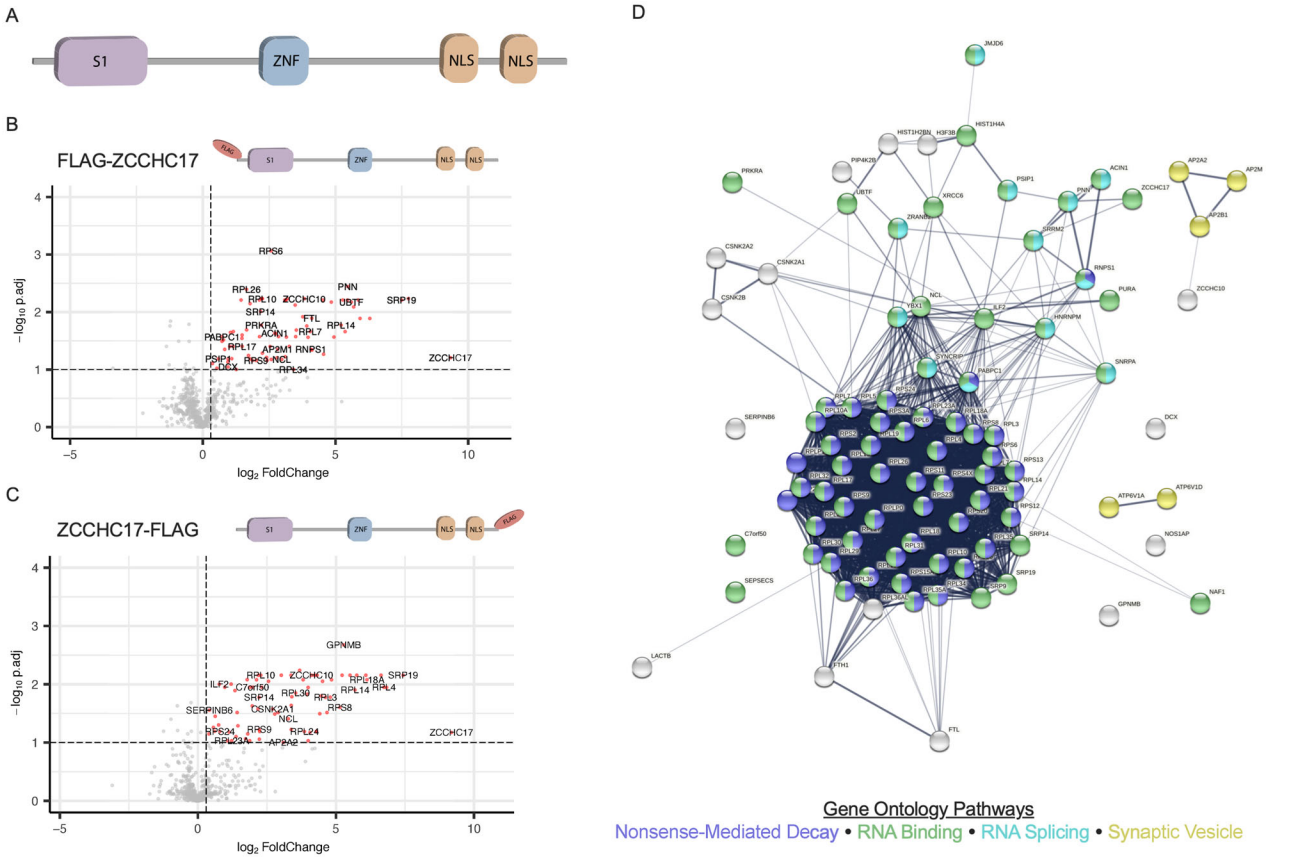

Figure 1. ZCCHC17 binding partners include RNA splicing, binding, and processing proteins. ***A***, ZCCHC17 protein domains include an S1 RNA-binding domain, a CCHC-type zinc-finger (ZnF) domain, and two nuclear localization signal (NLS) domains. ***B,C***, LC-MS/MS of bound proteins from anti-FLAG immunoprecipitation performed on human iPSC-derived neurons (Extended Data Fig. 1-1) differentiated for 75 d post-NPC expressing N- or C- terminal FLAG-tagged ZCCHC17 compared to control neurons (Extended Data Figs. 1-2, 1-3, 1-4). Volcano plots display $\log_2$-fold changes and FDR-corrected *p*-values defined with respect to protein abundance in control neurons ($n = 3$ for all groups); significant hits (adjusted $p < 0.1$ and $\log_2 FC > 0.3$) are highlighted in red (see Extended Data Table 1-1 for list of proteins immunoprecipitated with ZCCHC17). ***D***, STRING-derived known and predicted protein–protein interactions among ZCCHC17 binding partners, with relevant strongly enriched gene ontology pathways highlighted. ZCCHC17 binding partners were defined as the union of significant hits from both LC-MS/MS experiments and comprise 91 unique proteins in total.

Several of ZCCHC17's binding partners were also involved in the synaptic vesicle cycle (strength = 1.2; FDR-adjusted *p*-value for enrichment = 5.5×10^{-3}).

ZCCHC17 knockdown induces differential splicing that overlaps with known AD splicing abnormalities

The prevalence of RNA-splicing proteins among ZCCHC17's binding partners inspired further investigation of RNA-splicing alterations in hiPSC-derived neurons. Thus, we treated neurons with siRNAs targeting ZCCHC17 or nontargeting control siRNAs. ZCCHC17 was the most significantly downregulated of all differentially expressed genes (DEGs), with $\log_2 FC = -2.5$ (Extended Data Table 2-1), confirming robust knockdown (>80%). Alternative splicing analysis, conducted using the LeafCutter algorithm (Li et al., 2018), identified 732 differentially spliced intron clusters corresponding to 637 unique DSGs in the ZCCHC17 knockdown model (Fig. 2*A*, Extended Data Table 2-2). GO enrichment analysis revealed 69 significant GO terms enriched among ZCCHC17 knockdown DSGs, of which 11 were synaptic-related pathways (Extended Data Table 2-2). Top GO terms included "postsynaptic specialization organization" and "postsynaptic density organization" (adjusted *p*-values = 7.8×10^{-3} and 9.3×10^{-3}, respectively). Taken together, this suggests that ZCCHC17 affects splicing in a significant number of genes, among which synaptic targets are enriched.

We have previously demonstrated that ZCCHC17 levels are reduced early in AD, before significant astrogliosis or neuronal loss (Tomljanovic et al., 2018). To identify whether ZCCHC17 might alter the RNA processing of any synaptic genes affected in AD, differential splicing analysis was repeated using ROSMAP data comprising postmortem DLPFC brain tissue samples from 238 AD and 227 control patients (Raj et al., 2018). A total of 371 differentially spliced intron clusters were identified in ROSMAP AD samples, corresponding to 323 unique DSGs (Fig. 2*B*, Extended Data Table 2-2). GO enrichment analysis revealed 212 significant GO terms enriched among ROSMAP AD DSGs, of which 15 were synaptic-related pathways (Extended Data Table 2-2). "Postsynapse" was a top GO term (adjusted *p*-value = 9.6×10^{-7}).

When ZCCHC17 knockdown and ROSMAP AD splicing analyses were compared, 55 DSGs emerged in common (Fig. 2*C*). This represents 17% of all DSGs we detected in the bulk DLPFC RNA-seq data from ROSMAP and is statistically significant ($p = 1.0 \times 10^{-30}$ by Fisher's exact test). GO enrichment analysis of the 55 shared DSGs revealed 160 significant GO terms, of which 24 were synaptic-related pathways (Extended Data Table 2-2). Top GO terms enriched among

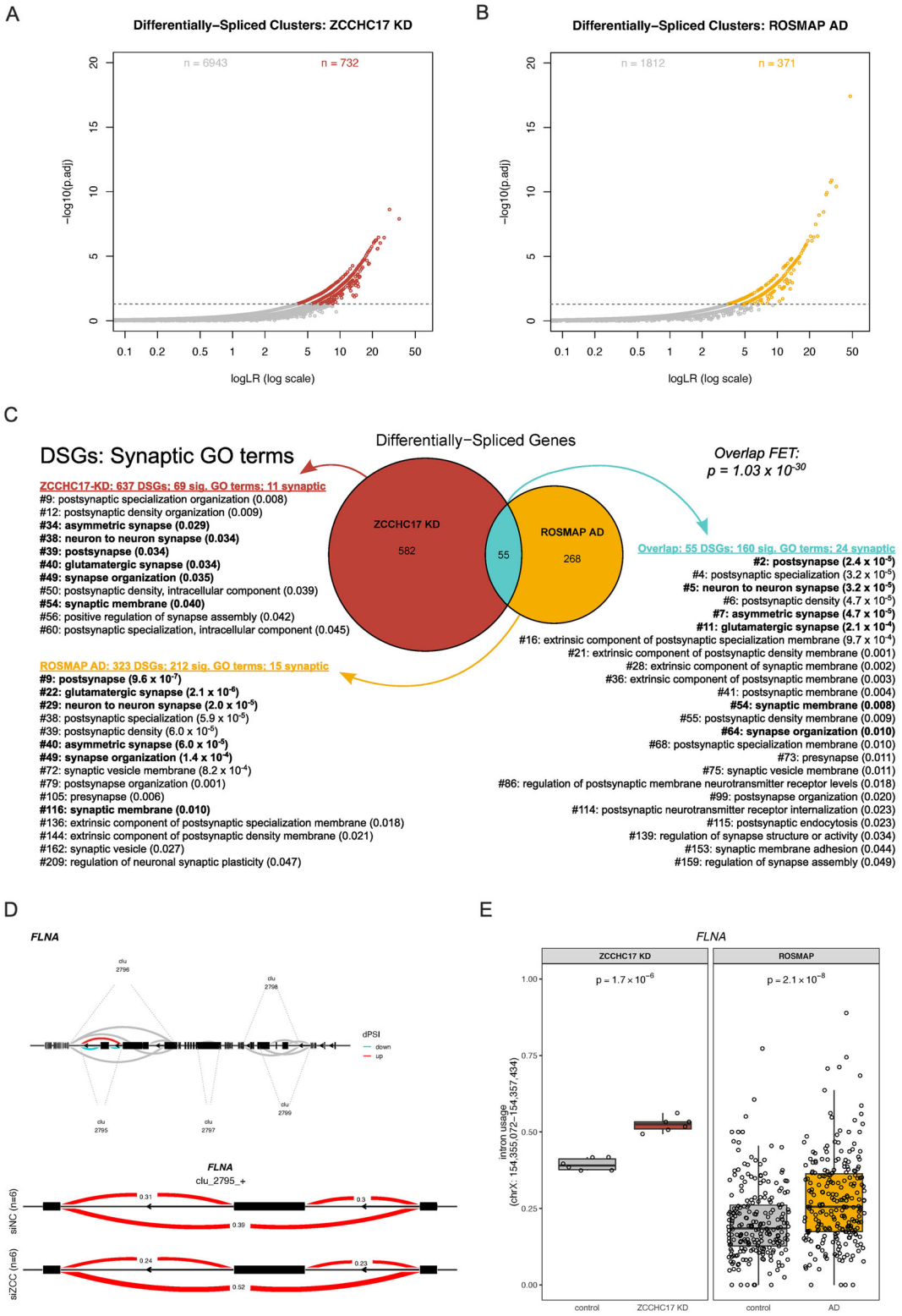

Figure 2. ZCCHC17 knockdown induces RNA-splicing alterations in AD-related genes. ***A***, 732 intron clusters exhibited differential splicing between ZCCHC17 knockdown ($n = 6$) and controls ($n = 6$) in human iPSC-derived neurons differentiated for 42 d post-NPC. ***B***, 371 intron clusters exhibited differential splicing between AD and control human DLPFC tissue samples from ROSMAP. ***C***, Differentially spliced genes (DSGs) in both ZCCHC17 knockdown neurons and AD human brain tissue are enriched for synaptic genes. There is a significant overlap in DSGs between the two data sets ($p = 1.0 \times 10^{-30}$ by Fisher's exact test). The 55 genes that are differentially spliced in both data sets are highly enriched for synaptic genes. ***D***, In ZCCHC17 knockdown neurons, FLNA is differentially spliced at cluster 2,795 ($p = 2.4 \times 10^{-9}$), corresponding to an exon-skipping event. All FLNA intron clusters identified by LeafCutter are shown in the top diagram. DeltaPSI (dPSI) is the difference in usage proportion between the two groups and is red or blue for introns with significantly increasing or decreasing dPSI, respectively. Clusters shown in gray did not change significantly. In the lower diagram, exons in cluster 2,795 are shown in black, with excision proportions for introns in both experimental groups shown in red. ***E***, Exon skipping occurs at the same location and to a similar degree in both ZCCHC17 knockdown neurons and AD human brain tissue, with significant changes in both contexts ($p = 1.7 \times 10^{-6}$ and 2.1×10^{-8}, respectively). See Extended Data Table 2-1 for list of differentially expressed genes in ZCCHC17 knockdown neurons, Extended Data Table 2-2 for lists of DSGs in ZCCHC17 knockdown neurons and ROSMAP AD brain tissue, and Extended Data Table 2-3 for a comparison of differential splicing across data sets.

overlapping DSGs included "postsynapse," "postsynaptic specialization," "neuron to neuron synapse," and "postsynaptic density" (adjusted p-values = 2.4×10^{-5}, 3.2×10^{-5}, 3.2×10^{-5}, and 4.7×10^{-5}, respectively). Examination of individual shared DSGs revealed similar patterns of differential splicing induced by ZCCHC17 knockdown and presence of AD. *FLNA* was the most dramatically affected synaptic DSG in both contexts; it was the most significant hit in the ZCCHC17 knockdown neuronal model and the third most significant hit in the ROSMAP AD analysis (Extended Data Table 2-2, Fig. 2*D*). Filamin A (FLNA) is the most common member of the filamin family of proteins, which bind to actin and are associated with synaptic activity. FLNA modulates ion channel abundance, controls aspects of membrane trafficking, and is involved in the hyperphosphorylation of tau through amyloid signaling (Noam et al., 2014; Burns and Wang, 2017). Differential splicing of FLNA occurs at the same intronic location and to a similar degree in both ZCCHC17 knockdown and AD contexts (Fig. 2*E*).

In total, 17 of the 55 DSGs in common between our ZCCHC17 knockdown model and ROSMAP AD were spliced in the same clusters and with the same direction of effect (Extended Data Table 2-3; clusters are defined by the LeafCutter algorithm as groups of introns that share splice sites and can be conceptualized as regions that contain multiple related splicing events). When restricted to this subset, the DSG overlap between ZCCHC17 knockdown and ROSMAP AD remains significant ($p = 0.002$ by Fisher's exact test), and synaptic genes are enriched in this subset (Extended Data Table 2-3). Another 17 of the 55 DSGs in common are spliced in different or nonoverlapping clusters, with the same splicing clusters detected in only four of these 17 genes. Empirical discovery of splice events in one data set are not always found in a comparative data set (Li et al., 2018), which underlines some of the existing challenges in splicing analysis with short-read RNA-seq data. Four of the 55 DSGs in common are spliced at the same clusters but with mixed effects. If we include all shared DSGs spliced in the same or mixed/nonoverlapping clusters, this totals 38 genes, with a Fisher's exact test p-value of 6.03×10^{-16}. Finally, 17 of the 55 DSGs in common are spliced in the same clusters but have an opposite effect in the two comparisons, and this subset of genes is not enriched for synaptic genes (Extended Data Table 2-3). Interestingly, if we focus on this subset, it is also significant using the Fisher's exact test (p-value = 0.002). It is unclear whether this subset of shared DSGs has a common function, but we speculate that it could generally represent compensation by neurons in adult brain in the setting of long-standing impaired ZCCHC17 function, in contrast to our acute knockdown model. In summary, a comparison between our ZCCHC17 knockdown neurons and AD brain tissue analyses shows a significant overlap in differential splicing with different degrees and directions, and a consistent impairment in synaptic gene splicing between the two. Taken together with our previous study demonstrating that ZCCHC17 is reduced in AD brains (Tomljanovic et al., 2018), this suggests that loss of ZCCHC17 function may explain a subset of splicing changes seen in AD brain tissue.

ZCCHC17 knockdown alters nonsense-mediated decay

As noted in Figure 1, ZCCHC17 also binds to 47 proteins involved in NMD. Although NMD has not been extensively examined in the context of AD, we investigated NMD in neurons following ZCCHC17 knockdown. dIF was quantified for isoforms with PTCs and those without. ZCCHC17 knockdown resulted in significantly increased ($p = 1.2 \times 10^{-11}$ by two-sided t test) expression of PTC-containing isoforms (which are sensitive to NMD), compared to isoforms lacking PTCs (Fig. 3*A*). More precisely, there is a sign skew in dIF by PTC status ($p = 3.5 \times 10^{-16}$ by Fisher's exact test). This relationship persists when considering only isoforms which exhibited individually significant dIF changes upon ZCCHC17 knockdown ($p = 2.8 \times 10^{-3}$ by two-sided t test and $p = 1.7 \times 10^{-4}$ by Fisher's exact test, Fig. 3*B*). Figure 3*C* illustrates an isoform switch in *VMP1*, a critical regulatory protein involved in the autophagy process that mediates autophagosome assembly via its ER contacts and maintains neuronal homeostasis (Zhao et al., 2017; Wang et al., 2020, 2021b), which has both NMD-insensitive and NMD-sensitive isoforms. Upon ZCCHC17 knockdown ("siZCC"), overall expression of *VMP1* decreases significantly and expression of the more stable NMD-insensitive isoforms also trends downward. In conjunction, expression of the NMD-sensitive isoform significantly increases, and the isoform fractions converge toward more similar expression levels. Additionally, the C-terminal domain of VMP1, which interacts with beclin-1 and is essential for its autophagy-promoting behavior (Vaccaro et al., 2008), is not present in the NMD-sensitive isoform. NMD-sensitive isoforms are more likely to undergo NMD and therefore less likely to be translated into functional proteins; thus, a shift toward NMD-sensitive isoforms for a specific gene could result in functional downregulation of that gene. Although we did not find a reduction in VMP1 protein after ZCCHC17 knockdown, p62 (a marker of autophagy dysfunction) (Ma et al., 2019) increased significantly, suggesting that autophagy in general is adversely affected (Extended Data Fig. 3-1).

We also investigated NMD in the ROSMAP RNA-seq data, but no significant change was detected in dIF values between NMD-sensitive and NMD-insensitive isoforms (Extended Data Fig. 3-2*B*). Note that below, we also examine NMD in a tau overexpression model, which does show a weak but significant shift in NMD (Extended Data Fig. 3-2*A*). Our overall impression from these data is that while ZCCHC17 knockdown and tau overexpression do cause a shift in NMD, the present analysis does not support a role for a NMD shift in AD brain tissue.

ZCCHC17 expression correlates with cognitive resilience

To identify whether ZCCHC17 levels may affect patient outcomes and disease progression in real-world data, we analyzed ZCCHC17 expression data in brain tissue samples from the ROSMAP study and compared its relationship to various cognitive metrics and the accumulation of AD-relevant neuropathologies. After filtering for sufficient RNA quality, 680 donor samples were analyzed from persons exhibiting varying degrees of cognitive decline and disease pathology. ZCCHC17 expression was found to correlate significantly and positively with all listed measures of cognitive function. Notably, these significant relationships were maintained after additionally controlling for various neuropathologies (Fig. 4*A*), although with a slight decrease in significance, suggesting that these associations are not entirely mediated through pathology. Apolipoprotein E4 (APOE4) is a major genetic risk factor of AD, with carriers of even one APOE4 allele having triple the risk of developing late-onset AD compared to patients without it (Uddin et al., 2019). As this patient cohort included a significant number of patients carrying at least one APOE4 allele (APOE4+), we also analyzed this data after splitting samples into groups based on APOE4 status to

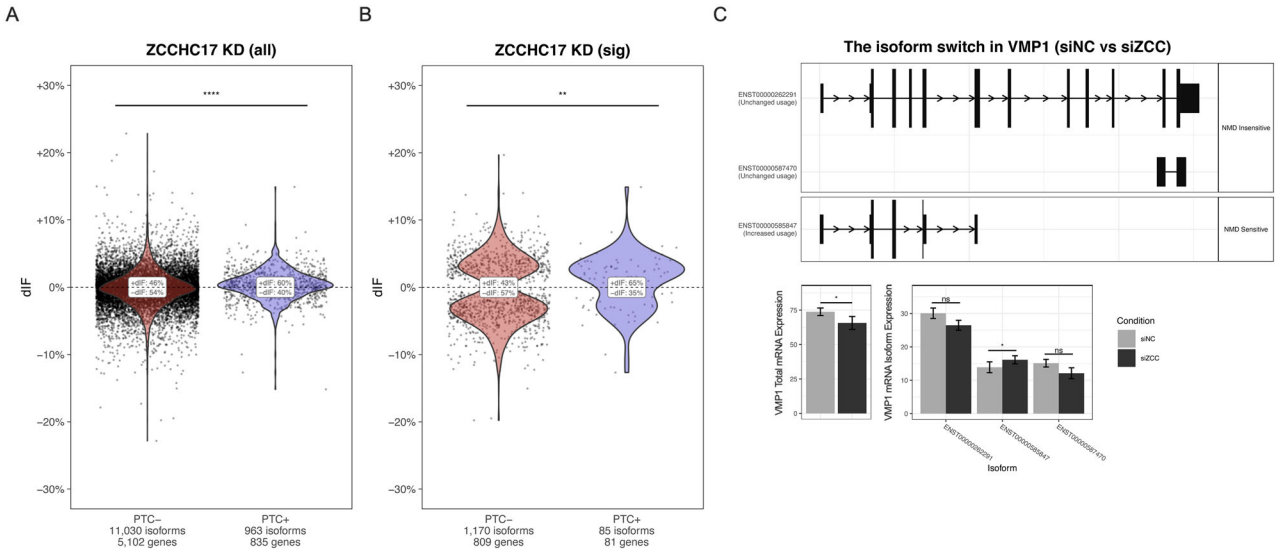

Figure 3. Nonsense-mediated decay is significantly altered following ZCCHC17 knockdown. ***A***, Isoforms containing premature termination codons (PTCs) exhibit significantly increased ($p = 1.2 \times 10^{-11}$) differential isoform fraction (dIF) in ZCCHC17 knockdown iPSC-derived neurons differentiated for 42 d post-NPC compared to isoforms lacking PTCs. Significant NMD-sensitive differential isoform fraction changes are also seen in tau-overexpressing neurons but not in ROSMAP AD data (Extended Data Fig. 3-2). ***B***, Among the subset of isoforms exhibiting significant changes in fractional expression following ZCCHC17 knockdown, there remains a significant increase ($p = 2.8 \times 10^{-3}$) in dIF in PTC+ versus PTC− isoforms. ***C***, VMP1 undergoes an isoform switch in ZCCHC17 knockdown neurons, exhibiting decreased expression of NMD-insensitive isoforms (which lack a PTC) and significantly increased expression (adjusted $p = 1.4 \times 10^{-2}$) of its NMD-sensitive isoform (which contains a PTC). Although we did not find a reduction in VMP1 protein after ZCCHC17 knockdown, p62 (a marker of autophagy dysfunction) (Ma et al., 2019) increased significantly, suggesting that autophagy in general is adversely affected (Extended Data Fig. 3-1). In the upper panel displaying VMP1 isoforms, the thin horizontal lines represent introns, vertical boxes represent exons, and arrows indicate the direction of transcription. Gene expression is derived from summing the isoform-level counts for all isoforms for that gene, and isoform data is derived from the isoform-level count data.

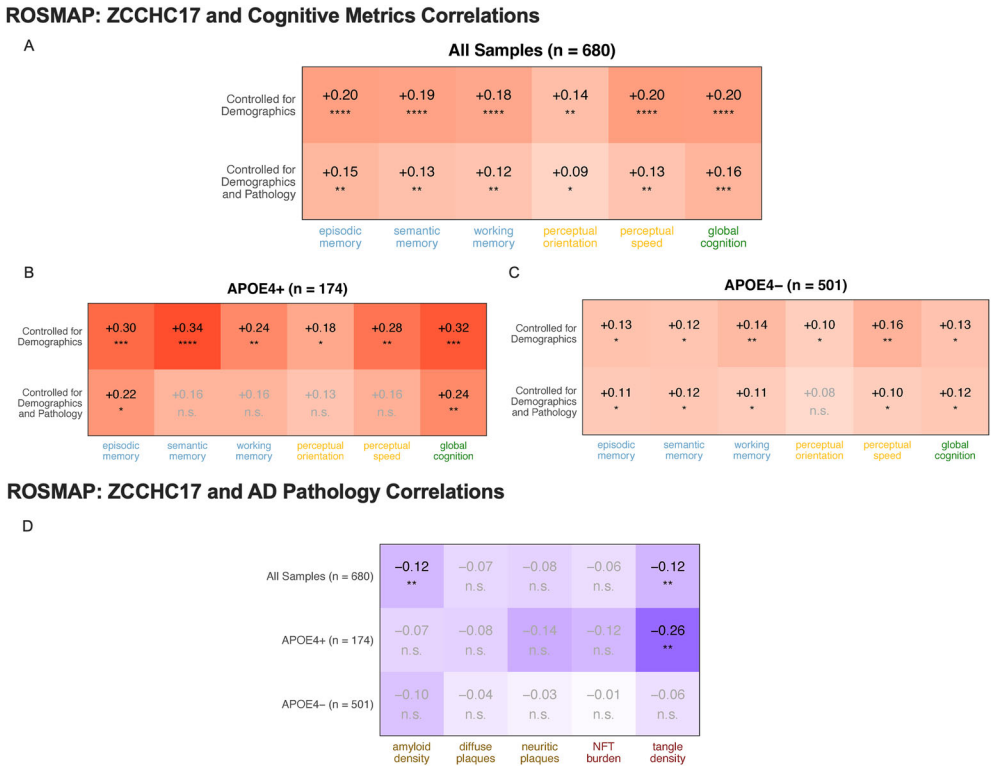

Figure 4. ZCCHC17 gene expression correlates with cognitive metrics and AD pathology. ***A***, ZCCHC17 expression correlates with cognitive metrics in ROSMAP DLPFC samples, whether these metrics are controlled for demographics alone or for both demographics and various measures of neuropathology. ***B,C***, Several cognitive metrics correlate strongly with ZCCHC17 expression in patients carrying an APOE4 allele (APOE4+) and moderately in patients without an APOE4 allele (APOE4−). ***D***, ZCCHC17 expression correlates weakly with amyloid density and tangle density in the full cohort, and strongly with tangle density in APOE4+ subjects. All values shown in heatmaps are Spearman correlation rho values, with red denoting positive correlations and blue denoting negative correlations, and the BH-adjusted significance of each correlation is indicated (*$p < 0.05$; **$p < 0.01$; ***$p < 0.001$; ****$p < 0.0001$; n.s., not significant). Predicted CNS expression of ZCCHC17 using PrediXcan analysis also correlates with cognitive resilience (Extended Data Fig. 4-1).

better understand the impact of this risk factor (Fig. 4*B*,*C*). ZCCHC17 expression was found to correlate significantly with all cognitive metrics in both APOE4+ and APOE4− groups. When pathology was controlled for in the APOE4+ group, this effect was lost for semantic memory, working memory, perceptual orientation, and perceptual speed, and attenuated for episodic memory and global cognition metrics (Fig. 4*B*). Note that the correlation between ZCCHC17 expression and cognition is maintained in the APOE4+ group when only controlling for demographics, suggesting that this is not a power issue per se, but rather an effect of pathology on this relationship in the APOE4+ cohort. Controlling for pathology in the APOE4− patient group had less of an effect on the relationship between ZCCHC17 expression and cognition, which was maintained across the majority of cognitive metrics (Fig. 4*C*). Global cognition and episodic memory were consistently correlated with ZCCHC17 expression across all sample types and subgroups.

Since we observed an effect of pathology on ZCCHC17 correlations with cognition in APOE4+ subjects, we next correlated ZCCHC17 expression with various measures of pathology. As seen in Figure 4*D*, ZCCHC17 expression weakly and negatively correlates with β-amyloid load in the midfrontal cortex, and the effect is lost when subjects are divided by APOE status. Interestingly, tangle density shows a strong negative correlation with ZCCHC17 expression that is specific for the APOE4+ group. Tau pathology has a well-known effect on cognition (Brier et al., 2016; Hansson et al., 2017), and this explains in part the relative loss of ZCCHC17 correlation with cognitive decline in APOE4+ subjects after regressing out the effect of various neuropathologies. It is unclear why this effect is APOE4-dependent, although several groups have demonstrated that APOE4 exacerbates neurodegeneration and neuronal death in the setting of tau pathology (Shi et al., 2017; Zhao et al., 2020). Whether this effect is mediated in part through ZCCHC17 transcriptional suppression should be investigated in future work (see Discussion).

In summary, the results shown in Figure 4 suggest that cognitive resilience in AD is linked to ZCCHC17 expression levels, and that this effect persists even after controlling for multiple neuropathologies (although APOE4 patients have a more complex picture). We previously found that ZCCHC17 protein levels decline early in the course of AD, before significant astrogliosis or neuronal loss (Tomljanovic et al., 2018). Taken together, one possible interpretation of these findings is that ZCCHC17 supports cognitive function in part through maintenance of RNA splicing/processing, and residual ZCCHC17 activity in AD brain is at least partially determinative of how well AD patients can maintain cognitive function, even in the setting of AD pathology.

The implication of these data is that elevated baseline ZCCHC17 expression levels may support cognitive resilience in the setting of progressive AD pathology. To test this hypothesis further, we used PrediXcan (Gamazon et al., 2015) to quantify predicted levels of ZCCHC17 expression, leveraging the GTEx database to build a model which we then applied to GWAS data. This methodology enables the use of GWAS/gene expression relationships across diverse tissues in a training set to predict genetically regulated levels of gene expression in a given tissue from subsequent GWAS data (Hohman et al., 2017; Dumitrescu et al., 2020). Higher predicted expression of ZCCHC17 across 15 tissues was associated with higher cognitive resilience (GBJ $p = 0.02$), including associations in heart tissue (atrial appendage $\beta = 0.17$, $p = 0.005$) and brain tissue (putamen $\beta = 0.09$, $p = 0.002$) that remained significant after correction for multiple comparisons. The results were slightly stronger when participants with AD were removed from the analytical models (GBJ $p = 0.004$), revealing additional associations in the tibial nerve ($\beta = 0.22$, $p = 0.001$), thyroid ($\beta = 0.15$, $p = 0.003$), pituitary ($\beta = 0.09$, $p = 0.01$), and colon ($\beta = 0.10$, $p = 0.02$) after correction for multiple comparisons.

One caveat to the above is that the association between predicted ZCCHC17 levels and cognitive resilience is mostly found in peripheral tissues in this analysis. However, this is likely due to the fact that these are the same tissues that are best powered in the models that generated these predictions (Dumitrescu et al., 2020). To address this, we determined whether predicted peripheral expression of ZCCHC17 associates with CNS expression using ROSMAP data. We found that higher predicted expression in five out of the six tissues that related to resilience also showed associations with higher measured ZCCHC17 expression in the brain (Extended Data Fig. 4-1), suggesting that even the predicted expression models built from peripheral tissues have relevance to the brain. A second caveat to the above is that the effect size is relatively small, with β coefficients in the 0.1–0.3 range. However, reported genetic effect sizes are often small in human disease trait analysis, even when highly significant (Andrews et al., 2023). This is probably due to many reasons, although the length of the causal chain between a genetic variant and a complex trait like resilience certainly plays a role. This genetic association between ZCCHC17 levels and resilience, even with a relatively small effect size, further supports our hypothesis that elevated ZCCHC17 levels are neuroprotective in the setting of AD pathology.

ZCCHC17 mRNA declines in neurons in AD

We have previously shown that ZCCHC17 protein declines in AD brain tissue (Tomljanovic et al., 2018), and the above analysis shows that maintenance of ZCCHC17 mRNA levels correlates with cognitive resilience in AD. We next sought to determine whether there is a cell-type-specific decline in ZCCHC17 mRNA levels in AD. We used recently published snRNA-seq data from prefrontal cortex (Sun et al., 2023) to determine whether ZCCHC17 declines in any of eight defined cell types. ZCCHC17 significantly declines in excitatory neurons (both CUX2+ upper-layer neurons and CUX2− lower-layer neurons; Fig. 5). ZCCHC17 does not significantly change in any other cell type, although it approaches significance in inhibitory neurons. This specificity is interesting in light of our proposed role of ZCCHC17 in AD and validates the excitatory iPSC neuronal model we used in this study.

Although ZCCHC17 has not been identified as an AD-associated risk gene through prior genome-wide SNP analysis, we also sought to determine whether there are any AD-risk variants in the ZCCHC17 loci that are nominally associated with AD, and if so, the level of significance of this association. We analyzed the summary statistics from a previously published AD GWAS (71,880 AD cases and 383,378 controls) (Jansen et al., 2019) to identify SNPs in ZCCHC17 that are associated with clinical AD. Two variants (rs59705505 at 3.73×10^{-6} and rs11336043 at 9.24×10^{-6}) are significant loci at $p < 1 \times 10^{-5}$. While not genome-wide significant at the widely used threshold of 5×10^{-8}, these variants are nominally significant in the NHGRI-EBI GWAS Catalog (Buniello et al., 2019). Although intriguing, it should be noted that ZCCHC17 is in a gene-dense region of the genome, and since these SNPs are not located within ZCCHC17, it is difficult to assign them unambiguously to ZCCHC17.

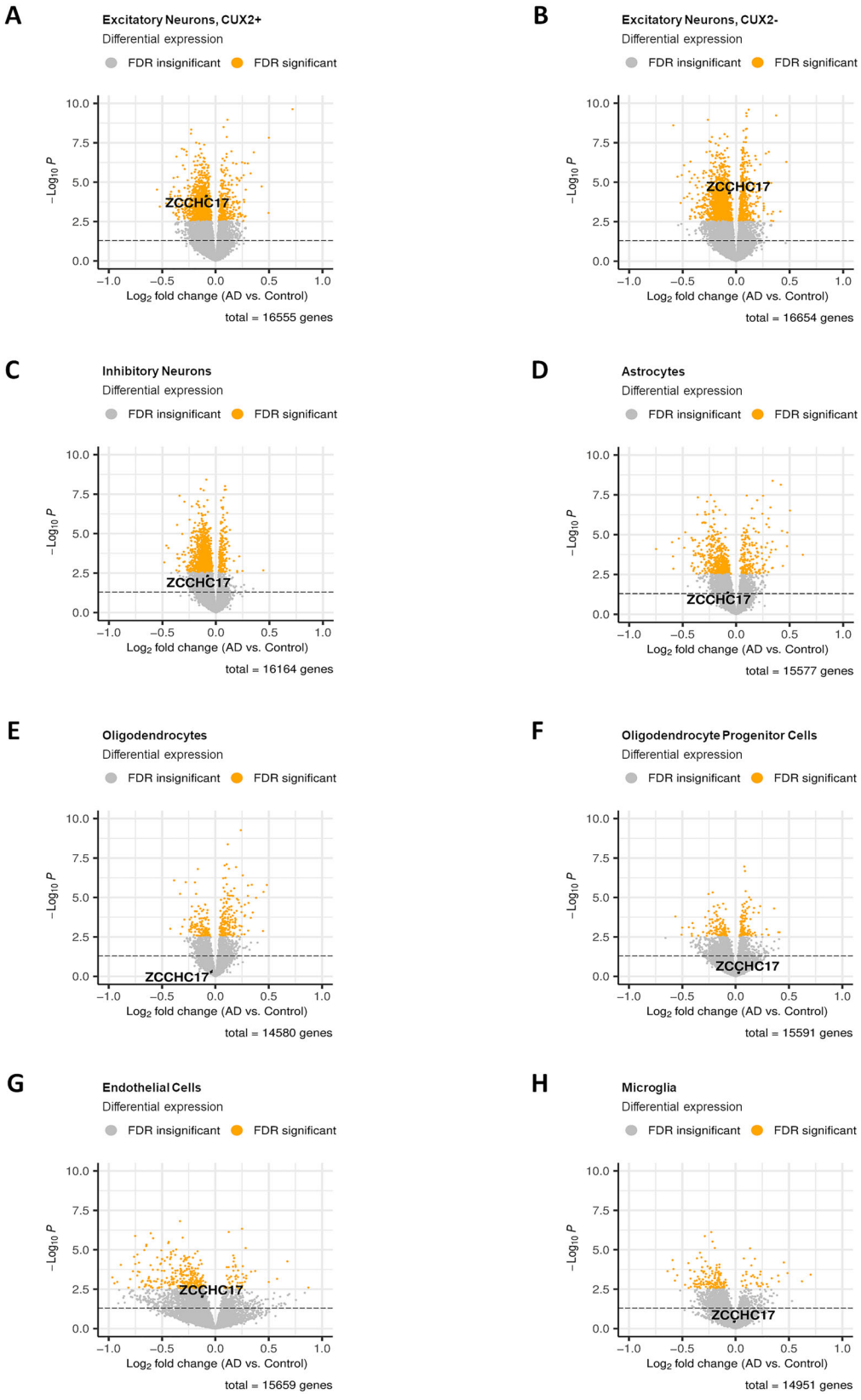

Figure 5. ZCCHC17 expression declines in neurons in AD. snRNA-seq data was used to assess cell-type-specific ZCCHC17 expression changes in AD. Shown are volcano plots for eight cell types. ***A,B***, Excitatory neurons (both upper-layer CUX2+ and lower-layer CUX2− excitatory neurons) show a significant decline in ZCCHC17 mRNA levels in AD. ***C–H***, A significant decline is not seen in any other cell type. Dotted line denotes p-value = 0.05. Genes with FDR-adjusted p-values of <0.05 are shown in orange, and the remaining genes are shown in gray.

ZCCHC17 and tau share common binding partners

Tau has been shown to bind to DNA and play a role in transcriptional regulation (Greenwood and Johnson, 1995; Hua et al., 2003). Tau also binds to RNA (Schröder et al., 1984; Dinkel et al., 2015), and tau overexpression has been linked to splicing abnormalities (Apicco et al., 2019; Hsieh et al., 2019; Montalbano et al., 2021). To investigate whether tau overexpression may play a causal role in ZCCHC17 dysfunction, ZCCHC17 binding partners were compared to published tau interactors in human postmortem brain tissue (Hsieh et al., 2019) (Extended Data Fig. 6-1). ZCCHC17 binding partners are significantly enriched [$p = 7.0 \times 10^{-14}$ by Fisher's exact test using the brain proteome as background (Johnson et al., 2020)] for tau binding partners, with 55% (50 proteins) of ZCCHC17 interactors being shared with tau (Extended Data Fig. 6-1*A*). These shared interactors include all synaptic vesicle proteins that interact with ZCCHC17, 42% of ZCCHC17 RNA-splicing proteins, 57% of ZCCHC17 RNA-binding proteins, and 66% of ZCCHC17 NMD proteins. When looking specifically at tau interactors in AD brains, ZCCHC17 binding partners are also significantly enriched ($p = 3.7 \times 10^{-10}$ by Fisher's exact test) for tau interactors, with 33% (30 proteins) of ZCCHC17 interactors shared with tau under AD conditions (Extended Data Fig. 6-1*B*). These shared interactors include all synaptic vesicle proteins that interact with ZCCHC17, 25% of ZCCHC17 RNA-splicing proteins, 32% of ZCCHC17 RNA-binding proteins, and 38% of ZCCHC17 NMD proteins.

Tau overexpression and ZCCHC17 knockdown in iPSC-derived neurons induce similar RNA-processing abnormalities

ZCCHC17 protein binding partners intersect with those of tau, suggesting that they may share overlapping functional roles in neurons. To investigate the effects of alterations in expression of tau on the generation of functional proteins and RNA, differential splicing analysis was conducted on previously published gene expression data from a tau overexpression model in human iPSC-derived neurons (Raj et al., 2018). In total, 99 differentially spliced clusters, corresponding to 91 unique DSGs, were identified when comparing tau overexpression samples with empty vector control samples (Fig. 6*A*, Extended Data Table 2-2). Of the 91 DSGs induced by tau overexpression, 17 were also affected following ZCCHC17 knockdown ($p = 1.05 \times 10^{-10}$ by Fisher's exact test; Fig. 6*B*). GO analysis of these 17 shared genes revealed significant enrichment in only two pathways: "cytoskeleton" (strength = 4.63, adjusted p-value = 6.9×10^{-2}) and "actin cytoskeleton" (strength = 11.76, adjusted p-value = 4.8×10^{-2}). In total, 13 out of the 91 tau overexpression DSGs were also affected in AD postmortem tissue from ROSMAP (Extended Data Table 2-2). Seven genes were significantly differentially spliced in all three data sets examined: ACTN4, AGRN, MYO6, NEO1, SEPTIN9, TACC2, and TSC22D3 (Extended Data Table 2-2). A-Actinin-4 (ACTN4) is a Ca^{2+}-sensitive actin-binding protein that promotes the remodeling of dendritic spines by metabotropic glutamate receptors (Walikonis et al., 2001; Kalinowska et al., 2015). The significant effect on splicing of ACTN4 in ZCCHC17 knockdown neurons stems from significant changes in clusters 3,931 (adjusted p-value = 1.2×10^{-2}) and 3,932 (adjusted p-value = 2.5×10^{-2}), with a greater effect size (loglr = 5.9) in cluster 3,931 (Fig. 6*C*). Tau overexpression neurons exhibited a significant splicing change in ACTN4 at the intron location matching cluster 3,931 (adjusted p-value = 4.2 10^{-2}), with a similar effect size (loglr = 5.4) (Fig. 6*D*). ACTN4 is also a significant DSG in the ROSMAP AD analysis, with high effect size for its affected clusters (loglr = 7.1 and 5.3), but these clusters correspond to unique intron locations in the ROSMAP data set and are not directly comparable.

When we compare splicing effects across the 17 DSGs in common between ZCCHC17 knockdown and tau overexpression neurons, only three genes are spliced in the same clusters and with the same direction of effect (Extended Data Table 2-3). Two genes are spliced in the same clusters but with opposite effect, and the remaining DSGs in common are spliced in non-overlapping clusters. The limited number of genes with similar splicing location and effect direction translates into nonsignificant overlap when we only consider these three genes ($p = 0.4$ by Fisher's exact test), although overlap is significant for the 15 out of 17 DSGs in common that are not spliced with a clearly opposing effect ($p = 8.02 \times 10^{-9}$ by Fisher's exact test). Similarly to the ZCCHC17 knockdown/ROSMAP comparison, most of the genes with nonoverlapping clusters between ZCCHC17 knockdown and tau overexpression neurons did not have all of the ZCCHC17 knockdown splice sites detected at a sufficient threshold for testing in the tau overexpression data (Extended Data Table 2-3; only 5 out of 12 DSGs with nonoverlapping clusters have all cluster splice sites from the ZCCHC17 knockdown found in the tau overexpression neurons). In addition, only 2 of the 12 DSGs with nonoverlapping clusters have all cluster splice sites from the tau overexpression neurons found in the ZCCHC17 knockdown neurons. This relatively low replication of splicing clusters across data sets is interesting, especially since in this instance we are comparing two sets of human neuronal cultures, as opposed to neuronal cultures versus brain autopsy tissue when we compare our ZCCHC17 knockdown to ROSMAP data. Although it is possible that many of the clusters detected in the ZCCHC17 knockdown simply do not exist in the tau overexpression neuronal cultures (and vice versa), it is also possible that we are not powered to identify and test all splicing clusters given the relatively small sample sizes of these two experiments. We can nonetheless conclude that the significant overlap in DSGs between these two models should motivate additional work to understand these splicing abnormalities in the setting of ZCCHC17 knockdown and tau overexpression.

Since tau binding partners included a large number of NMD proteins (Extended Data Fig. 6-1), we also investigated the NMD mechanism in the tau overexpression data. Although the effect was weaker than observed in ZCCHC17 knockdown neurons, tau overexpression neurons exhibited a significant increase in dIF for PTC-containing isoforms ($p = 6.6 \times 10^{-3}$ by two-sided t test) as well as a significant positive skew in dIF for PTC-containing isoforms ($p = 0.03$ by Fisher's exact test), indicating a similar shift in RNA processing (Extended Data Fig. 3-2). This previously unreported effect of tau overexpression on RNA processing, while weak, suggests that tau may be affecting RNA metabolism through multiple mechanisms related to RNA splicing. As noted above, we also investigated this mechanism in the ROSMAP AD data set, but no significant change was detected in dIF values between NMD-sensitive and NMD-insensitive isoforms (Extended Data Fig. 3-2), suggesting that if NMD changes are relevant in AD, their effects are either weak or difficult to detect in autopsy brain tissue.

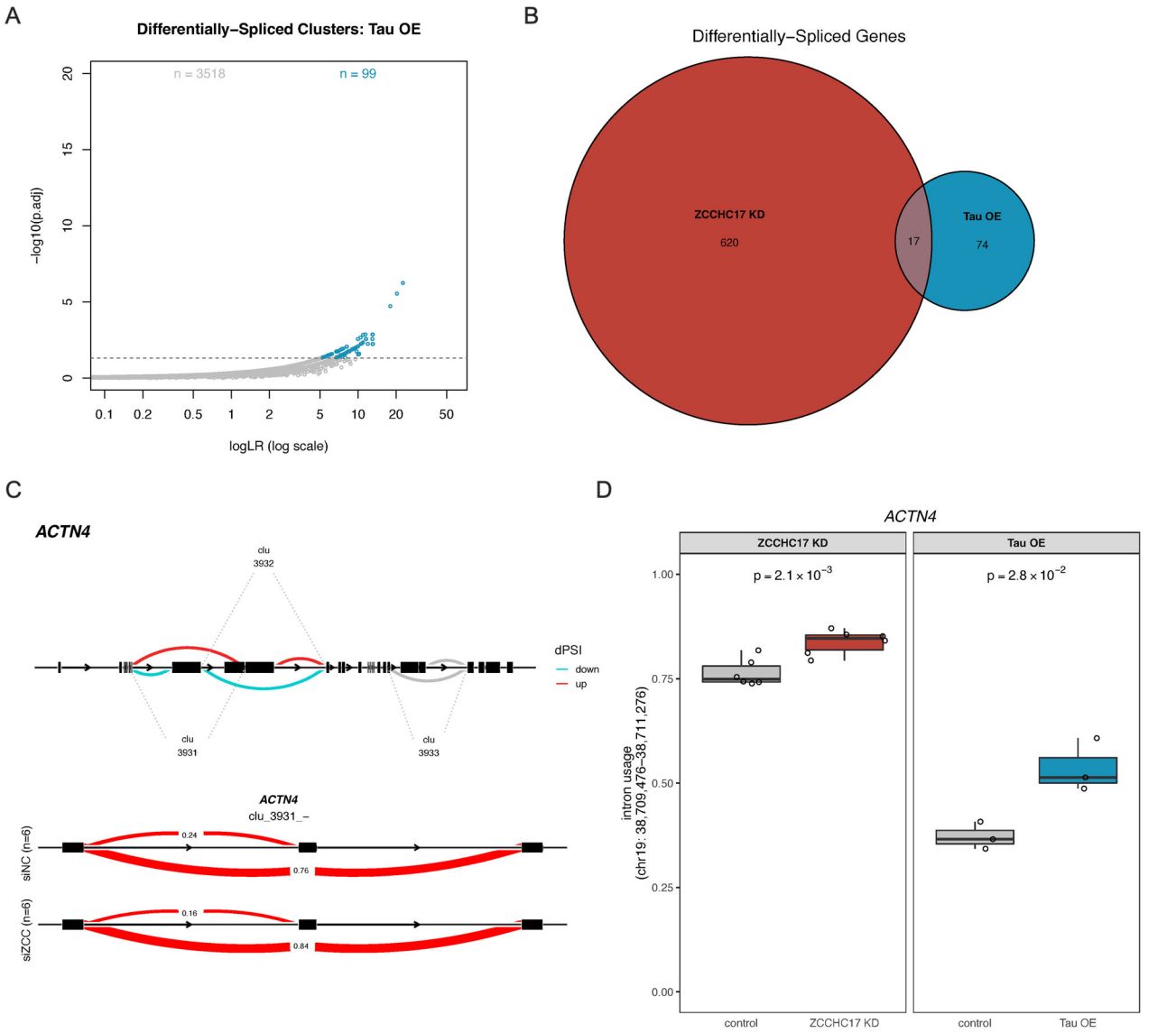

Figure 6. Tau overexpression induces RNA-splicing and processing alterations similar to ZCCHC17 knockdown-dependent changes. ZCCHC17 and tau share a significant number of binding partners (Extended Data Fig. 6-1), including shared RNA-splicing interactors, which motivated a comparison of RNA-processing abnormalities in tau overexpression and ZCCHC17 knockdown neurons. ***A***, 99 intron clusters exhibited differential splicing between tau overexpression iPSC-derived neurons ($n = 3$) and controls ($n = 3$). ***B***, 17 DSGs are shared between ZCCHC17 knockdown neurons ("ZCCHC17 KD," 637 DSGs) and tau overexpression neurons ("Tau OE," 91 DSGs). ***C***, In ZCCHC17 knockdown neurons, ACTN4 is differentially spliced at clusters 3,931 (adjusted $p = 1.2 \times 10^{-2}$) and 3,932 (adjusted $p = 2.5 \times 10^{-2}$), with significantly decreasing dPSI in blue and significantly increasing dPSI in red. Other clusters identified by LeafCutter for ACTN4 are shown in gray. The alteration in cluster 3,931 corresponds to an exon-skipping event, with usage proportions of significantly changing introns shown in red in the lower panel. Exons are shown in black. ***D***, Alternative splicing occurs at the same location and to a similar degree in both ZCCHC17 knockdown neurons and tau overexpression neurons, with significant changes in both ($p = 2.1 \times 10^{-3}$ and 2.8×10^{-2}, respectively). See Extended Data Table 2-2 for list of differentially spliced genes in tau overexpression neurons and Extended Data Table 2-3 for a comparison of differential splicing across data sets.

Discussion

In this study, we have further explored the function of ZCCHC17, originally identified by our group as a transcriptional regulator whose dysfunction in AD may contribute to dysregulation of synaptic gene expression (Tomljanovic et al., 2018). We define ZCCHC17's interactions at the RNA processing and protein level and compare its impacts across multiple disease-relevant models. Our co-IP study provides a comprehensive list of proteins, which interact with ZCCHC17 in human neurons under basal conditions, and defines relevant groups of interactions based on protein function. The network of proteins which bind to ZCCHC17 includes synaptic proteins as well as many involved in the regulation and stability of RNA and downstream proteins, specifically from RNA splicing, RNA binding, and NMD pathways. RNA metabolism proteins have been implicated in several neurodegenerative diseases; amyotrophic lateral sclerosis (ALS) and autism have been linked to the dysfunction of RNA-binding proteins (Parikshak et al., 2016; Kapeli et al., 2017), and pathologic RNA-protein aggregates have been observed in ALS and inclusion body myopathy (Ramaswami et al., 2013; Taylor et al., 2016). In late-onset AD, tau has been shown to interact with RNA (Schröder et al., 1984; Dinkel et al., 2015), RNA-binding proteins (Broccolini et al., 2000; Bai et al., 2013; Gunawardana et al., 2015; Hsieh et al., 2019), and the ribosome (Ding, 2005; Koren et al., 2020). ZCCHC17 has previously

been found to interact with other transcriptional regulators (Chang et al., 2003) as well as splicing factors (Ouyang, 2009; Lin et al., 2017), but our work directly shows these interactions in human neurons and provides a more comprehensive view of its interactions with other proteins.

We evaluated and quantified differential splicing in human neurons following ZCCHC17 knockdown and compared these alterations to those observed in brain tissue from AD patients. We show that ZCCHC17 knockdown leads to dysregulation of mRNA splicing across a broad range of categories (including synaptic genes) and that these splicing abnormalities significantly overlap with splicing abnormalities in AD brain tissue. Pre-mRNA splicing plays a major role in the development of many human diseases; at least 20–30% of disease-causing mutations are associated with aberrant splicing (Wang and Cooper, 2007; Lim et al., 2011). Neurodegenerative diseases in particular have been linked to specific splicing alterations, including *MAPT* exon 10 splice site mutations in frontotemporal dementia and parkinsonism linked to chromosome 17 (FTDP-17) (Hutton et al., 1998; Trabzuni et al., 2012) and potentially *SCNA* isoforms in Parkinson's disease (Oueslati, 2016; Kaji et al., 2020). In late-onset AD, intron retention increases to levels significantly beyond those observed in physiological aging, and widespread disruption of splicing mechanisms alters the brain transcriptome (Faustino, 2003; Vaquero-Garcia et al., 2016; Raj et al., 2018; Adusumalli et al., 2019). The DSGs in our ZCCHC17 knockdown model which overlap with those in AD brain tissues are enriched for synaptic genes, further supporting the view that loss of ZCCHC17 function in AD may contribute to synaptic dysfunction.

Alternative splicing is a complex phenomenon that alters RNA and protein magnitude and diversity. The downstream effects of dysregulated alternative splicing are likely much broader and of a greater magnitude when splicing defects significantly disrupt RNA and protein expression for a prolonged period of time, for example, over the decades of pathologic progression which precede clinical onset of AD (Perrin et al., 2009; Jack, 2011). How ZCCHC17 dysfunction interacts with ongoing RNA metabolic defects in AD and how this contributes to cognitive dysfunction are interesting questions. Indeed, ZCCHC17 is a relatively unstudied protein, and the work detailed here elevates the importance of further investigating its role in health and disease. As noted in one of the original papers that discovered ZCCHC17, the protein contains a number of potential phosphorylation sites, including 10 for protein kinase C, 6 for casein kinase II, and 2 for cAMP-dependent kinase (Chang et al., 2003). Although early work found that cytoplasmic ZCCHC17 co-fractionates with ribosomes (Gueydan et al., 2002), recent studies have focused on its nuclear function and revealed that it possesses a diverse range of functions relevant to both mRNA (Lin et al., 2017) and rRNA (Lin et al., 2019) processing. This has led some to suggest that ZCCHC17 may play a broad role in coordinating and maintaining cell homeostasis (Lin et al., 2017).

The effect of ZCCHC17 expression on cognition is both interesting and understandable given these wide-ranging effects on neuronal health. Our group previously showed that ZCCHC17 protein levels decline early in the course of AD, before significant gliosis or neuronal loss (Tomljanovic et al., 2018). Interestingly, we show here that ZCCHC17 mRNA levels, while sensitive to some aspects of AD pathology, correlate with a broad range of cognitive metrics even after controlling for neuropathology. One possible interpretation of these data is that the level of functional ZCCHC17 protein declines in AD, and higher ZCCHC17 expression in some individuals can partially buffer this effect. This interpretation is further supported by our PrediXcan analysis of ZCCHC17 expression, which shows that predicted levels of ZCCHC17 correlate with cognitive resilience in patients with documented AD pathology on imaging. Although we have presented evidence supporting an impact of ZCCHC17 on cognitive function in this study, the exact mechanism for this impact is not clear. While ZCCHC17's role in regulating synaptic gene expression is an obvious candidate, the broader influence that ZCCHC17 may exert on neuronal health should not be ignored, and ZCCHC17 loss of function may contribute to neurodegeneration through a variety of mechanisms. Indeed, while in this paper we have focused on ZCCHC17 interactors involved in RNA processing (which comprise the majority of the interactors we identified), we also found that proteins involved in synaptic vesicle cycling, autophagy, and stress granule formation interact with ZCCHC17. We have not explored the relevance of these findings in this study, but they warrant further investigation in future studies of ZCCHC17 and its contribution to neurodegeneration.

We also uncovered a potential interaction between ZCCHC17 and tau, initially by investigating the overlap of protein binding partners via our co-IP study, which suggests that tau accumulation in AD could disrupt functionally relevant protein binding partners of ZCCHC17. A hypothesized sequestration of the network of proteins supporting ZCCHC17 function by AD-related tau would likely interfere with its ability to regulate RNA processing, as >70% of these overlapping proteins are involved in RNA splicing, RNA binding, or NMD pathways. Our follow-up alternative splicing and NMD analysis found similarities between our ZCCHC17 knockdown model and published tau overexpression data at the RNA-processing level, which may reflect downstream effects of this protein-level relationship. Future work will need to examine whether ZCCHC17 function is affected by tau in AD brain tissue through sequestration of ZCCHC17 interactors. Interestingly, we also found a strong correlation between ZCCHC17 gene expression and neurofibrillary tangle burden in patients carrying an APOE4 allele, which also impacts the link between ZCCHC17 expression and cognition in APOE4 carriers (particularly semantic memory, working memory, and perceptual memory) after regressing out the effect of AD pathology. Additional investigation is necessary to further elucidate the relationship between ZCCHC17, tau, and APOE.

Finally, while the focus of this paper has been on splicing, a number of ribosomal proteins were also discovered to interact with ZCCHC17. While the relationship between tau and the ribosome and its subsequent contribution to neurodegeneration has generated increasing interest over recent years, the tau–ribosome interaction in neurons bearing NFT pathology was demonstrated decades ago in early ultrastructural studies and in studies utilizing human tauopathy cohorts (Nelson and Saper, 1995; Piao et al., 2002). Since then, interactome studies have found that tau associates with over 50 ribosomal proteins (Gunawardana et al., 2015). Experiments conducting subcellular fractionation to isolate ER-associated ribosomes have also shown that both pathological and nonpathological tau are capable of binding these organelles, and that this interaction is stronger in AD brains compared to healthy controls (Meier et al., 2016). Importantly, the consequences of this relationship have started to become clearer in recent years, with evidence in tauopathy mouse models suggesting that ribosomal protein synthesis and translation inversely correlate with levels of pathological tau (Evans et al., 2019, 2021, Koren et al., 2019).

These observations were also seen in AD brain samples, where tau was found to pathologically interact with a critical regulator of translation, ribosomal protein S6, resulting in reduced protein synthesis under its translational control (Koren et al., 2019). Impaired synthesis of synaptic proteins following tau–ribosome interaction has also been reported (Meier et al., 2016), indicating that not only does this robust association impair ribosomal function and hence protein synthesis and translation, but also may contribute to synaptic dysfunction as seen in disease. Future work will need to determine whether a tau-mediated ribosome dysfunction may in part be due to the disruption of an association between ribosomes and ZCCHC17.

Abbreviations

AD, Alzheimer's disease; NPC, neural progenitor cells; PBS, phosphate-buffered saline; SDS-PAGE, sodium dodecyl sulfate–polyacrylamide gel electrophoresis; TBST, Tris-buffered saline with 0.1% Tween; MS, mass spectrometry; FDR, false discovery rate; hiPSC, human-induced pluripotent stem cell; ROSMAP, Rush Memory and Aging Project; DSGs, differentially spliced genes; GO, gene ontology; PTCs, premature termination codons; RIN, RNA integrity number; PMI, postmortem interval; NMD, nonsense-mediated decay; dIF, differential isoform fraction; BH, Benjamini–Hochberg; GWAS, genome-wide association study; DEGs, differently expressed genes; DLPFC, dorsolateral prefrontal cortex; GBJ, Generalized Berk–Jones.

Ethics Approval and Consent to Participate

All human cell line work was performed on de-identified cell lines and approved by the Columbia University Institutional Review Board (IRB).

Data Availability Statement

Newly generated RNA-seq data have been deposited in GEO (https://www.ncbi.nlm.nih.gov/geo/, GSE199241) and are publicly available as of the date of publication. ROSMAP RNA-seq data is available via the AMP-AD data portal through Synapse (https://www.synapse.org/#!Synapse:syn3219045) and the RADC Research Resource Sharing Hub (https://www.radc.rush.edu).

References

Adusumalli S, Ngian ZK, Lin WQ, Benoukraf T, Ong CT (2019) Increased intron retention is a post-transcriptional signature associated with progressive aging and Alzheimer's disease. Aging Cell 18:e12928.

Anderson P, Kedersha N (2008) Stress granules: the Tao of RNA triage. Trends Biochem Sci 33:141–150.

Andrews SJ, Renton AE, Fulton-Howard B, Podlesny-Drabiniok A, Marcora E, Goate AM (2023) The complex genetic architecture of Alzheimer's disease: novel insights and future directions. EBioMedicine 90:104511.

Apicco DJ, Zhang C, Maziuk B, Jiang L, Ballance HI, Boudeau S, Ung C, Li H, Wolozin B (2019) Dysregulation of RNA splicing in tauopathies. Cell Rep 29:4377–4388.e4.

Bai B, et al. (2013) U1 small nuclear ribonucleoprotein complex and RNA splicing alterations in Alzheimer's disease. Proc Natl Acad Sci U S A 110:16562–16567.

Bennett DA, Buchman AS, Boyle PA, Barnes LL, Wilson RS, Schneider JA (2018) Religious orders study and rush memory and aging project. J Alzheimers Dis 64:S161–S189.

Brier MR, et al. (2016) Tau and abeta imaging, CSF measures, and cognition in Alzheimer's disease. Sci Transl Med 8:338ra366.

Broccolini A, Engel WK, Alvarez RB, Askanas V (2000) Paired helical filaments of inclusion-body myositis muscle contain RNA and survival motor neuron protein. Am J Pathol 156:1151–1155.

Buniello A, et al. (2019) The NHGRI-EBI GWAS catalog of published genome-wide association studies, targeted arrays and summary statistics 2019. Nucleic Acids Res 47:D1005–D1012.

Burns LH, Wang H-Y (2017) Altered filamin A enables amyloid beta-induced tau hyperphosphorylation and neuroinflammation in Alzheimer's disease. Neuroimmunol Neuroinflamm 4:263.

Chang W-L, Lee D-C, Leu S, Huang Y-M, Lu M-C, Ouyang P (2003) Molecular characterization of a novel nucleolar protein, pNO40. Biochem Biophys Res Commun 307:569–577.

Chen G, et al. (2011) Chemically defined conditions for human iPSC derivation and culture. Nat Methods 8:424–429.

Colangelo V, Schurr J, Ball MJ, Pelaez RP, Bazan NG, Lukiw WJ (2002) Gene expression profiling of 12633 genes in Alzheimer hippocampal CA1: transcription and neurotrophic factor down-regulation and up-regulation of apoptotic and pro-inflammatory signaling. J Neurosci Res 70:462–473.

Cox JR, Neuhauser N, Michalski A, Scheltema RA, Olsen JV, Mann M (2011) Andromeda: a peptide search engine integrated into the MaxQuant environment. J Proteome Res 10:1794–1805.

De Jager PI, et al. (2018) A multi-omic atlas of the human frontal cortex for aging and Alzheimer's disease research. Sci Data 5:180142.

Ding Q (2005) Ribosome dysfunction is an early event in Alzheimer's disease. J Neurosci 25:9171–9175.

Dinkel PD, Holden MR, Matin N, Margittai M (2015) RNA binds to tau fibrils and sustains template-assisted growth. Biochemistry 54:4731–4740.

Dumitrescu L, et al. (2020) Genetic variants and functional pathways associated with resilience to Alzheimer's disease. Brain 143:2561–2575.

Evans HT, Benetatos J, van Roijen M, Bodea LG, Gotz J (2019) Decreased synthesis of ribosomal proteins in tauopathy revealed by non-canonical amino acid labelling. EMBO J 38:e101174.

Evans HT, Taylor D, Kneynsberg A, Bodea LG, Gotz J (2021) Altered ribosomal function and protein synthesis caused by tau. Acta Neuropathol Commun 9:110.

Faustino NA (2003) Pre-mRNA splicing and human disease. Genes Dev 17:419–437.

Gamazon ER, et al. (2015) A gene-based association method for mapping traits using reference transcriptome data. Nat Genet 47:1091–1098.

Greenwood JA, Johnson GVW (1995) Localization and in situ phosphorylation state of nuclear tau. Exp Cell Res 220:332–337.

Gueydan C, Wauquier C, De Mees C, Huez G, Kruys V (2002) Identification of ribosomal proteins specific to higher eukaryotic organisms. J Biol Chem 277:45034–45040.

Gunawardana CG, Mehrabian M, Wang X, Mueller I, Lubambo IB, Jonkman JE, Wang H, Schmitt-Ulms G (2015) The human tau interactome: binding to the ribonucleoproteome, and impaired binding of the proline-to-leucine mutant at position 301 (P301L) to chaperones and the proteasome. Mol Cell Proteomics 14:3000–3014.

Hansson O, Grothe MJ, Strandberg TO, Ohlsson T, Hagerstrom D, Jogi J, Smith R, Scholl M (2017) Tau pathology distribution in Alzheimer's disease corresponds differentially to cognition-relevant functional brain networks. Front Neurosci 11:167.

Hohman TJ, Dumitrescu L, Cox NJ, Jefferson AL (2017) Genetic resilience to amyloid related cognitive decline. Brain Imaging Behav 11:401–409.

Hsieh Y-C, et al. (2019) Tau-mediated disruption of the spliceosome triggers cryptic RNA splicing and neurodegeneration in Alzheimer's disease. Cell Rep 29:301–316.e10.

Hua Q, He R-Q, Haque N, Qu M-H, Del Carmen Alonso A, Grundke-Iqbal I, Iqbal K (2003) Microtubule associated protein tau binds to double-stranded but not single-stranded DNA. Cell Mol Life Sci 60:413–421.

Hu K, Yu J, Suknuntha K, Tian S, Montgomery K, Choi K-D, Stewart R, Thomson JA, Slukvin II (2011) Efficient generation of transgene-free induced pluripotent stem cells from normal and neoplastic bone marrow and cord blood mononuclear cells. Blood 117:e109–e119.

Huttlin EL, et al. (2017) Architecture of the human interactome defines protein communities and disease networks. Nature 545:505–509.

Hutton M, et al. (1998) Association of missense and 5′-splice-site mutations in tau with the inherited dementia FTDP-17. Nature 393:702–705.

Jack CR (2011) Evidence for ordering of Alzheimer disease biomarkers. Arch Neurol 68:1526.

Jansen IE, et al. (2019) Genome-wide meta-analysis identifies new loci and functional pathways influencing Alzheimer's disease risk. Nat Genet 51:404–413.

Johnson ECB, et al. (2020) Large-scale proteomic analysis of Alzheimer's disease brain and cerebrospinal fluid reveals early changes in energy

metabolism associated with microglia and astrocyte activation. Nat Med 26:769–780.
Kaji S, Maki T, Ishimoto T, Yamakado H, Takahashi R (2020) Insights into the pathogenesis of multiple system atrophy: focus on glial cytoplasmic inclusions. Transl Neurodegener 9:7.
Kalinowska M, Chávez AE, Lutzu S, Castillo PE, Bukauskas FF, Francesconi A (2015) Actinin-4 governs dendritic spine dynamics and promotes their remodeling by metabotropic glutamate receptors. J Biol Chem 290: 15909–15920.
Kapeli K, Martinez FJ, Yeo GW (2017) Genetic mutations in RNA-binding proteins and their roles in ALS. Hum Genet 136:1193–1214.
Koren SA, et al. (2019) Tau drives translational selectivity by interacting with ribosomal proteins. Acta Neuropathol 137:571–583.
Koren SA, Galvis-Escobar S, Abisambra JF (2020) Tau-mediated dysregulation of RNA: Evidence for a common molecular mechanism of toxicity in frontotemporal dementia and other tauopathies. Neurobiol Dis 141:104939.
Lambert SA, Jolma A, Campitelli LF, Das PK, Yin Y, Albu M, Chen X, Taipale J, Hughes TR, Weirauch MT (2018) The human transcription factors. Cell 172:650–665.
Li YI, Knowles DA, Humphrey J, Barbeira AN, Dickinson SP, Im HK, Pritchard JK (2018) Annotation-free quantification of RNA splicing using LeafCutter. Nature Genet 50:151–158.
Li X, Long J, He T, Belshaw R, Scott J (2015) Integrated genomic approaches identify major pathways and upstream regulators in late onset Alzheimer's disease. Sci Rep 5:12393.
Liang WS, et al. (2008) Altered neuronal gene expression in brain regions differentially affected by Alzheimer's disease: a reference data set. Physiol Genomics 33:240–256.
Lim KH, Ferraris L, Filloux ME, Raphael BJ, Fairbrother WG (2011) Using positional distribution to identify splicing elements and predict pre-mRNA processing defects in human genes. Proc Natl Acad Sci U S A 108:11093–11098.
Lin YM, Chu PH, Li YZ, Ouyang P (2017) Ribosomal protein pNO40 mediates nucleolar sequestration of SR family splicing factors and its overexpression impairs mRNA metabolism. Cell Signal 32:12–23.
Lin YM, Chu PH, Ouyang P (2019) Ectopically expressed pNO40 suppresses ribosomal RNA synthesis by inhibiting UBF-dependent transcription activation. Biochem Biophys Res Commun 516:381–387.
Loring JF, Wen X, Lee JM, Seilhamer J, Somogyi R (2001) A gene expression profile of Alzheimer's disease. DNA Cell Biol 20:683–695.
Ma S, Attarwala IY, Xie XQ (2019) SQSTM1/p62: a potential target for neurodegenerative disease. ACS Chem Neurosci 10:2094–2114.
Meier S, et al. (2016) Pathological tau promotes neuronal damage by impairing ribosomal function and decreasing protein synthesis. J Neurosci 36: 1001–1007.
Montalbano M, Jaworski E, Garcia S, Ellsworth A, McAllen S, Routh A, Kayed R (2021) Tau modulates mRNA transcription, alternative polyadenylation profiles of hnRNPs, chromatin remodeling and spliceosome complexes. Front Mol Neurosci 14:742790.
Mostafavi S, et al. (2018) A molecular network of the aging human brain provides insights into the pathology and cognitive decline of Alzheimer's disease. Nat Neurosci 21:811–819.
Nelson PT, Saper CB (1995) Ultrastructure of neurofibrillary tangles in the cerebral cortex of sheep. Neurobiol Aging 16:315–323.
Noam Y, Ehrengruber MU, Koh A, Feyen P, Manders EMM, Abbott GW, Wadman WJ, Baram TZ (2014) Filamin A promotes dynamin-dependent internalization of hyperpolarization-activated cyclic nucleotide-gated type 1 (HCN1) channels and restricts Ih in hippocampal neurons. J Biol Chem 289:5889–5903.
Oueslati A (2016) Implication of alpha-synuclein phosphorylation at S129 in synucleinopathies: what have we learned in the last decade? J Parkinsons Dis 6:39–51.
Ouyang P (2009) SRrp37, a novel splicing regulator located in the nuclear speckles and nucleoli, interacts with SC35 and modulates alternative pre-mRNA splicing in vivo. J Cell Biochem 108:304–314.
Parikshak NN, et al. (2016) Genome-wide changes in lncRNA, splicing, and regional gene expression patterns in autism. Nature 540:423–427.
Perrin RJ, Fagan AM, Holtzman DM (2009) Multimodal techniques for diagnosis and prognosis of Alzheimer's disease. Nature 461:916–922.
Piao YS, Hayashi S, Wakabayashi K, Kakita A, Aida I, Yamada M, Takahashi H (2002) Cerebellar cortical tau pathology in progressive supranuclear palsy and corticobasal degeneration. Acta Neuropathol 103:469–474.
Pre D, Nestor MW, Sproul AA, Jacob S, Koppensteiner P, Chinchalongporn V, Zimmer M, Yamamoto A, Noggle SA, Arancio O (2014) A time course analysis of the electrophysiological properties of neurons differentiated from human induced pluripotent stem cells (iPSCs). PLoS One 9:e103418.
Raj T, et al. (2018) Integrative transcriptome analyses of the aging brain implicate altered splicing in Alzheimer's disease susceptibility. Nat Genet 50: 1584–1592.
Ramaswami M, Taylor JP, Parker R (2013) Altered ribostasis: RNA-protein granules in degenerative disorders. Cell 154:727–736.
Schröder HC, Bernd A, Zahn RK, Müller WEG (1984) Binding of polyribonucleotides and polydeoxyribonucleotides to bovine brain microtubule protein: age-dependent modulation via phosphorylation of high-molecular-weight microtubule-associated proteins and tau proteins. Mech Ageing Dev 24:101–117.
Shevchenko A, Tomas H, Havlis J, Olsen JV, Mann M (2006) In-gel digestion for mass spectrometric characterization of proteins and proteomes. Nat Protoc 1:2856–2860.
Shi Y, et al. (2017) ApoE4 markedly exacerbates tau-mediated neurodegeneration in a mouse model of tauopathy. Nature 549:523–527.
Siskova Z, et al. (2014) Dendritic structural degeneration is functionally linked to cellular hyperexcitability in a mouse model of Alzheimer's disease. Neuron 84:1023–1033.
Smith DL, Pozueta J, Gong B, Arancio O, Shelanski M (2009) Reversal of long-term dendritic spine alterations in Alzheimer disease models. Proc Natl Acad Sci U S A 106:16877–16882.
Song S, Ashok A, Williams D, Kaufman M, Duff K, Sproul A (2021) Efficient derivation of excitatory and inhibitory neurons from human pluripotent stem cells stably expressing direct reprogramming factors. Curr Protoc 1: e141.
Sun J, et al. (2019) CRISPR/Cas9 editing of APP C-terminus attenuates β-cleavage and promotes α-cleavage. Nat Commun 10:53.
Sun N, et al. (2023) Single-nucleus multiregion transcriptomic analysis of brain vasculature in Alzheimer's disease. Nat Neurosci 26:970–982.
Szklarczyk D, et al. (2019) STRING v11: protein–protein association networks with increased coverage, supporting functional discovery in genome-wide experimental datasets. Nucleic Acids Res 47:D607–D613.
Taylor JP, Brown RH, Cleveland DW (2016) Decoding ALS: from genes to mechanism. Nature 539:197–206.
Teich AF, Nicholls RE, Puzzo D, Fiorito J, Purgatorio R, Fa M, Arancio O (2015) Synaptic therapy in Alzheimer's disease: a CREB-centric approach. Neurotherapeutics 12:29–41.
Tomljanovic Z, Patel M, Shin W, Califano A, Teich AF (2018) ZCCHC17 is a master regulator of synaptic gene expression in Alzheimer's disease. Bioinformatics 34:367–371.
Topol A, Tran NN, Brennand KJ (2015) A guide to generating and using hiPSC derived NPCs for the study of neurological diseases. J Vis Exp 96:e52495.
Trabzuni D, et al. (2012) MAPT expression and splicing is differentially regulated by brain region: relation to genotype and implication for tauopathies. Hum Mol Genet 21:4094–4103.
Trinchese F, Liu S, Battaglia F, Walter S, Mathews PM, Arancio O (2004) Progressive age-related development of Alzheimer-like pathology in APP/PS1 mice. Ann Neurol 55:801–814.
Uddin MS, Kabir MT, Al Mamun A, Abdel-Daim MM, Barreto GE, Ashraf GM (2019) APOE and Alzheimer's disease: evidence mounts that targeting APOE4 may combat Alzheimer's pathogenesis. Mol Neurobiol 56: 2450–2465.
Vaccaro MI, Ropolo A, Grasso D, Iovanna JL (2008) A novel mammalian trans-membrane protein reveals an alternative initiation pathway for autophagy. Autophagy 4:388–390.
Vanderweyde T, et al. (2016) Interaction of tau with the RNA-binding protein TIA1 regulates tau pathophysiology and toxicity. Cell Rep 15:1455–1466.
Vaquero-Garcia J, Barrera A, Gazzara MR, GonzáLez-Vallinas J, Lahens NF, Hogenesch JB, Lynch KW, Barash Y (2016) A new view of transcriptome complexity and regulation through the lens of local splicing variations. Elife 5:e11752.
Walikonis RS, Oguni A, Khorosheva EM, Jeng C-J, Asuncion FJ, Kennedy MB (2001) Densin-180 forms a ternary complex with the α-subunit of Ca2 +/calmodulin-dependent protein kinase II and α-actinin. J Neurosci 21: 423–433.
Wang M, et al. (2021a) Transformative network modeling of multi-omics data reveals detailed circuits, key regulators, and potential therapeutics for Alzheimer's disease. Neuron 109:257–272.e14.
Wang P, Chen X, Wang Y, Jia C, Liu X, Wang Y, Wu H, Cai H, Shen H-M, Le W (2021b) Essential role for autophagy protein VMP1 in maintaining

neuronal homeostasis and preventing axonal degeneration. Cell Death Dis 12:116.
Wang GS, Cooper TA (2007) Splicing in disease: disruption of the splicing code and the decoding machinery. Nat Rev Genet 8:749–761.
Wang P, Kou D, Le W (2020) Roles of VMP1 in autophagy and ER-membrane contact: potential implications in neurodegenerative disorders. Front Mol Neurosci 13:42.
Yu J, et al. (2007) Induced pluripotent stem cell lines derived from human somatic cells. Science 318:1917–1920.
Yu J, Hu K, Smuga-Otto K, Tian S, Stewart R, Slukvin II, Thomson JA (2009) Human induced pluripotent stem cells free of vector and transgene sequences. Science 324:797–801.
Zhao YG, et al. (2017) The ER-localized transmembrane protein EPG-3/VMP1 regulates SERCA activity to control ER-isolation membrane contacts for autophagosome formation. Mol Cell 67:974–989.e6.
Zhao J, et al. (2020) APOE4 exacerbates synapse loss and neurodegeneration in Alzheimer's disease patient iPSC-derived cerebral organoids. Nat Commun 11:5540.